CO6-1 Radioresistance Mechanisms Acquired by Adaptive Evolution and their Evolutionary Mechanisms III

T. Saito

Institute for Integrated Radiation and Nuclear Science, Kyoto University

INTRODUCTION: Organisms have evolved diverse forms by adapting to various environmental conditions, and some can survive in hostile environments. Studying these adaptive mechanisms can provide meaningful information regarding the evolution and biological diversity of organisms. Some radioresistant bacteria are highly resistant to ionizing radiation [1]. The mechanism through which bacteria resist ionizing radiation is an interesting research subject considering the adaptive mechanisms employed by organisms in nature. To elucidate the mechanisms of radioresistance in these organisms, the biological defense mechanisms against external stress must be investigated at the molecular level. However, studies on naturally occurring radioresistant organisms are particularly challenging, owing to limited knowledge of their genetic and biochemical properties. Therefore, in this study, radioresistant *Escherichia coli*, whose wild-type genetic and biochemical characteristics have been elucidated in detail, were generated via an adaptive evolution experiment using gamma rays as the selective pressure, and the characteristics of the evolved radioresistant *E. coli* were compared with those of the wild type. Previously, radioresistant *E. coli* have been generated with a 7.9-fold resistance compared with wild-type *E. coli* [2, 3, 4]. This report describes the differences in gene expression status between wild-type and radioresistant *E. coli*.

EXPERIMENTS: Extraction of total RNA and RNA sequencing : Total RNA was extracted from *E. coli* cells using RNAiso Plus (Takara) and further purified using NucleoSpin RNA Clean-up XS (Macherey-Nagel). The quality of total RNA was evaluated and confirmed using an Agilent 2100 Bioanalyzer (Agilent Technologies). rRNA was removed from the total RNA using a Ribo-Zero Magnetic Kit (Gram-Negative Bacteria) (Illumina). A sequence library was prepared from the resulting RNA using a TruSeq Stranded mRNA Sample Prep Kit (Illumina). The quality of the sequence library was evaluated and confirmed using an Agilent 2100 Bioanalyzer. Sequence analysis was performed using NovaSeq 6000 (Illumina), NovaSeq 6000 S4 Reagent Kit (Illumina), and NovaSeq Xp 4-Lane Kit (Illumina). Gene expression levels were analyzed using Genedata Profiler Genome (Genedata) and STAR [5]. All procedures were performed according to the manufacturer's instructions.

Analysis of gene expression status: In the analysis, gene expression data with “fragments per kilobase of transcript per million mapped fragments” values less than 1 for all samples from the two groups compared were filtered to eliminate noise data. Differentially expressed genes (DEGs) in radioresistant *E. coli* compared with wild-type *E. coli* were identified using Welch's t-test and correction for multiple testing using the Benjamini and Hochberg method (BH method) [6]. Furthermore, Kyoto Encyclopedia of Genes and Genomes (KEGG) pathway analysis of DEGs in radioresistant *E. coli* relative to wild-type *E. coli* was performed using the Database for Annotation, Visualization and Integrated Discovery bioinformatics resources ver.6.8.

Statistical analysis: Welch's t-test and the BH method were used to identify DEGs among many genes, and a q-value of less than 0.05 was considered significant. The Expression Analysis Systematic Explorer score was used to test for significance in KEGG pathway analysis, and a P-value of less than 0.05 was considered significant [7].

RESULTS: KEGG pathway analysis revealed that genes involved in metabolism-related pathways are enriched in genes up-regulated in radioresistant *E. coli* compared with wild-type *E. coli*. Previously, the high expression of genes involved in survival, cell recovery, DNA repair, and response after stress exposure was found to be involved in the radioresistance of radioresistant *E. coli* [3, 4]. Alterations in the expression of metabolism-related genes described in this report are likely to optimize the intracellular environment for survival, cell recovery, DNA repair, and response after irradiation by regulating the state of intracellular molecules.

REFERENCES:

[1] T. Saito, Viva Origino, **30** (2007) 85-92.
[2] T. Saito, KURNS ProgressReport 2019, (2020) 211.
[3] T. Saito, KURNS ProgressReport 2020, (2021) 162.
[4] T. Saito, KURNS ProgressReport 2021, (2022) 158.
[5] A. Dobin *et al.*, Bioinfomatics, **29** (2013) 15-21.
[6] Y. Benjamini and Y. Hochberg, J. R. Statist. Soc. B, **57** (1995) 289-300.
[7] D. W. Huang *et al.*, Nat. Protoc. **4** (2009) 44-57.

CO6-2 Integrated approach for structural analysis of a biomacromolecule in a polydispersed solution using analytical ultracentrifugation and small-angle X-ray scattering

K. Morishima[1], Y. Yunoki[1], A. Okuda[1], M. Shimizu[1], N. Sato[1], R. Inoue[1], M. Sugiyama[1]

[1]*Institute for Integrated Radiation and Nuclear Science, Kyoto University*

INTRODUCTION:

Small-angle X-ray and neutron scatterings (SAXS and SANS; collectively called SAS) offer overwhelming opportunities for structural analysis of a biomacromolecule in solution. Especially, state-of-the-art computational analyzing methods for SAS offer a high resolution three-dimensional structural model and/or its dynamics in the solution. To build a reliable structural model through the advanced analyses, it is essential to obtain the precise SAS profile from only a target biomacromolecule. Hence, a sample should be purified to be a monodisperse solution prior to a SAS measurement. Nevertheless, non-specific oligomers, namely aggregates, often remain in the solution even after purification. Even if the weight fraction of aggregates is a few %, the experimental SAS profile is deteriorated by them. As the result, an incorrect structural model is built as the target biomacromolecule: This is the fatal problem on the structural analysis with SAS.

To overcome this problem, a new data-reduction method, "AUC-SAS"[1], has been developed with integration of analytical ultracentrifugation (AUC) and SAS. AUC provides the weight fractions and molecular weights of all components in solution without destruction of aggregates and complexes. AUC-SAS derives the scattering profile of a target biomacromolecule from the deteriorated experimental profile using the information provided by AUC. However, the first designed AUC-SAS (first-AUC-SAS)[1] is constrained by the weight fraction of the aggregates (less than approximately 10 %). In this study, we improved AUC-SAS, which is applicable to samples with relatively large weight fraction of aggregates (> 10 %).

EXPERIMENTS:

As the demonstration of AUC-SAS, bovine serum albumin, apoferritin, catalase, lysozyme, ovalbumin, and ribonuclease A were subjected to the SAXS and AUC measurements.

SAXS measurements were carried out with NANOPIX (Rigaku). AUC measurements were conducted with a ProteomeLab XL-I (Beckman Coulter). All measurements were conduceted at 25 ºC.

RESULTS:

AUC-SAS derives the scattering profile of a target molecule through following steps;

Step 1. Derivation of forward scattering intensity.

Step 2. Derivation of scattering profile in high q region.

Step 3. Connection of forward scattering and scattering profile in high q region with Guinier approximation.

On the Step 2 in the first-AUC-SAS, the scattering profile in high q region for the target molecules is approximated to be identical with that for aggregates because it is not different in the inner local structure between the monomer and the aggregates in the sample for a general SAS measurement. However, we found that this approximation leads to the error in the target scattering profile for the samples with relatively large weight fraction of aggregates (> 10 %).

We improved the procedure of the Step 2 with carefully reconsidering the scattering profile of an aggregate. To express the scattering profile of an aggregate, we applied the random flight model. Consequently, the improved-AUC-SAS offered the correct scattering profile of the target molecule even for the sample with ~20% of weight fraction of aggregates: The improved-AUC-SAS was demonstrated to offer the consistent result with size exclusion chromatography (SEC)-SAXS for various proteins (bovine serum albumin, apoferritin, catalase, lysozyme, ovalbumin, and ribonuclease A).[2]

Because AUC-SAS does not require a large amount of sample or a very highly intensive instrument, such as synchrotron-light SAXS, it has a potential to be applied to laboratory-based SAXS. Additionally, AUC-SAS is applicable to also SANS which faces the same aggregation problem as well as SAXS. Indeed, we confirmed that the improved-AUC-SANS successfully works with the SANS data measured with SANS-U at JRR-3. Finally, we developed the software of the improved-AUC-SAS for broad SAS users (available at [http://www.rri.kyoto-u.ac.jp/NSBNG/activity.html]) [2].

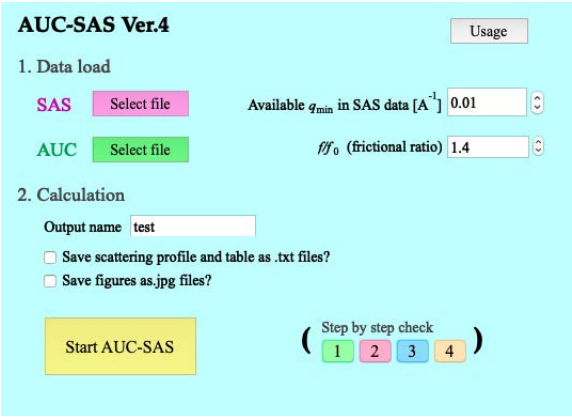

Fig. 1. Interface of AUC-SAS software on the Igor Pro.

REFERENCES:

[1] K. Morishima *et al.,* Commun. Biol., **3** (2020) 294.

[2] K. Morishima *et al.,* J. Appl. Crystallogr., (2023) in press.

R4010

CO6-3 Mutational and environmental effects on the dynamic conformational distributions of Lys48- linked di-ubiquitin chains

K. Kato, M. Yagi-Utsumi, S. Yanaka, H. Yagi, K. Morishima[1], R. Inoue[1], N. Sato[1] and M. Sugiyama[1]
Graduate School of Pharmaceutical Sciences, Nagoya City University
[1]*Institute for Integrated Radiation and Nuclear Science, Kyoto University*

INTRODUCTION: In multidomain proteins, individual domains connected by flexible linkers are dynamically rearranged upon ligand binding and sensing changes in environmental factors, such as pH and temperature. We characterize dynamic domain rearrangements of Lys48-linked ubiquitin (Ub) chains as models of multidomain proteins in which molecular surfaces mediating intermolecular interactions are involved in intramolecular domain–domain interactions [1, 2]. Using NMR and other biophysical techniques, we characterized dynamic conformational interconversions of diUb between open and closed states regarding solvent exposure of the hydrophobic surfaces of each Ub unit, which serve as binding sites for various Ub-interacting proteins. We found that the hydrophobic Ub-Ub interaction in diUb was reinforced by cysteine substitution of Lys48 of the distal Ub unit because of interaction between the cysteinyl thiol group and the C-terminal segment of the proximal Ub unit. In contrast, the replacement of the isopeptide linker with an artificial ethylenamine linker minimally affected the conformational distributions.

Small-angle neutron scattering (SANS) and small-angle X-ray scattering (SAXS) are powerful techniques for the structural characterization of biomolecular complexes. Here, we attempted to elucidate the time scale of the transit domain motions of the Lys48-linked diUb chain collaborated with SAXS and molecular dynamics (MD) simulation.

EXPERIMENTS: We prepared the Lys48-linked diUb. We performed SEC-SAXS of Lys48-linked diUb chain at 283 K using the laboratory-based SAXS instrument, NANOPIX equipped with a HyPix-6000 (Rigaku Corporation, Japan).

RESULTS: We obtained the SAXS profile of di-Ub (Fig. 1, light blue circle) and determined the radius of gyration (R_g) using Guinier analysis, which yielded $R_{g,exp}$=19.9±0.2 Å. To investigate whether the crystal structure differs from that of di-Ub in solution, we used Pepsi-SAXS [3] to calculate a SAXS curve from the crystal structure, which is shown as the black line in Figure 1. The R_g calculated from the SAXS curve was $R_{g,xtal}$=16.9 Å, indicating a structural difference between the crystal and solution states of di-Ub. This difference is likely due to domain motion in solution.

To further investigate this, we conducted all-atom molecular dynamics (MD) simulation for 100 ns at 283 K using GROMACS with the AMBER99-SB [4] force field and the crystal structure as the initial structure. From the trajectories of MD simulation, we extracted structures every 10 ps and calculated SAXS curves for each structure. We then averaged these curves to obtain the SAXS curve shown in red in Fig. 1. The R_g calculated from this curve was R_{g,MD_ave}=17.4 Å, with an average sum of squared residuals of $\chi^2_{MD\_ave}$=4.2, which was better than the scattering profile obtained from the crystal structure alone $R_{g,xtal}$=16.9 Å, χ^2_{xtal}=5.6).

We further plan to optimize the force field parameters and identify the domain motion of di-Ub in order to improve the reproducibility of the experimental data.

The conformational interconversion of Ub chains offers a unique design framework in Ub-based protein engineering not only for developing biosensing probes but also for allowing new opportunities for the allosteric regulation of multidomain proteins.

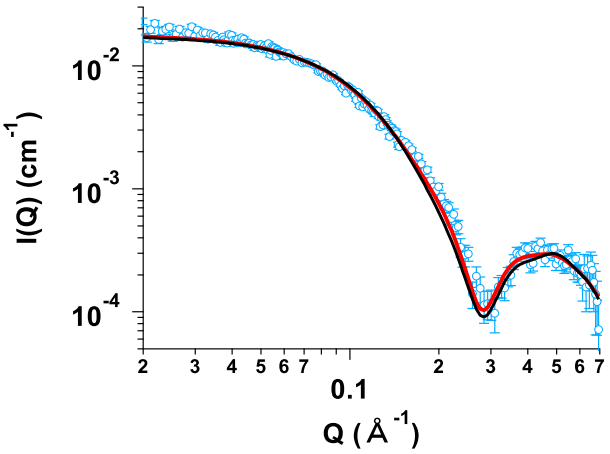

Fig. 1. Experimental SAXS curve of di-Ub (light blue circles), SAXS curve calculated from the crystal structure of di-Ub (black line), and ensemble average of SAXS curves for each structure for all atoms MD (red line).

REFERENCE:

[1] M. Hiranyakorn *et al.*, Int. J. Mol. Sci., **21** (2020) 5351. (doi) 10.3390/ijms21155351.
[2] M. Hiranyakorn *et al.*, Int. J. Mol. Sci., **24** (2023) 6075. (doi) 10.3390/ijms24076075.
[3] S. Grudinin *et al.*, Acta. Cryst., **D73** (2017) 449. (doi) 10.1107/S2059798317005745.
[4] V. Hornak *et al.*, *Proteins*, **65** (2006) 712. (doi) 10.1002/prot.21123.

CO6-4 Evaluation of BPA-Uridine conjugates as Smart Drugs for BNCT

K. Tanabe,[1] T. Nishihara,[1] and M. Suzuki[2]

[1]*Department of Chemistry and Biological Science, College of Science and Engineering, Aoyama Gakuin University*
[2]*Institute for Integrated Radiation and Nuclear Science, Kyoto University*

INTRODUCTION:

Modified nucleobases are widely used in vivo as functional materials.[1] Recently, we have shown that nucleobases can be utilized as an efficient solubilizer and carrier of hydrophobic drugs. We have employed uridine as a functional solubilizer and carrier for poorly soluble compounds BPA and constructed BPA-uridine conjugate for boron neutron capture therapy (BNCT). We had found that irradiation in the presence of the conjugate markedly enhanced the cytotoxicity of radiation.

In this study, we evaluated their cytotoxic effect against several tumor cells. In vivo study revealed that the conjugate selectively accumulated into tumor tissues and showed high cytotoxic effects upon thermal neutron irradiation.

EXPERIMENTS:

Preparation of BPA-uridine conjugate. BPA was added to the aqueous solution of uridine under basic conditions to solubilize the conjugate. After the BPA was dissolved in the aqueous solution, the resulting solution was neutralized and then subjected to in vivo experiments.

Neutron capture therapy to SAS tumor models. SAS cells in matrigel (1×10^6 cells per mouse) were subcutaneously inoculated into the right thighs of BALB/c nude mice. The tumors were allowed to grow ~1.0 month. The mouse was injected with fructose-BPA or uridine-BPA (250 mg/kg). The mice were placed in acrylic which were secured on a 5-mm-thick thermoplastic plate that contained 40 weight % (wt %) of ^{6}LiF (96% 6Li) to block thermal neutrons and had a circular hole in the center. The thigh containing the tumor was stretched over the hole, and the tumor was irradiated with epi-/thermal neutrons for 50 min, 1 h after the injection. The tumor size was measured by a caliper, and tumor volume (V) was calculated using the following equation: $V = ab^2/2$, where a and b are the major and minor axes, respectively.

RESULTS:

Last year, we found that the BPA-uridine complex dissolved smoothly in water, and it exhibited high cytotoxicity toward A549 cells under thermal neutron irradiation. Therefore, in this study, we further determined its cytotoxicity toward other tumor cells such as SAS and SCCVII cells. We evaluated the cytotoxicity of BPA-uridine conjugate against these cells, which were exposed to neutron (1 MW) in the presence of aqueous solution consisted of BPA and uridine and then incubated at 37 ˚C. After wash, cell survival was determined by WST assay. Figure 1 compares cell survivals in the presence and absence of BPA-uridine after irradiation. The cytotoxic effect of radiation was significantly enhanced when the cells were irradiated in the presence of BPA-uridine. It is likely that BPA is effectively activated in the cells and thereby exhibits high cytotoxicity against tumor cells upon irradiation.

We also evaluated the cytotoxic effect of BPA-uridine using tumor tissue planted in mice. To determine whether the BPA-uridine conjugate is effective in vivo, we administered this conjugate to BALB/cAJcl nude mice with SAS tumors. SAS cells were transplanted into BALB/cAJcl nude mice (n = 3 per group) and allowed to grow until the tumor size was about 200 mm^3. The conjugate was then administered subcutaneously and changes in tumor size after thermal neutron irradiation were recorded. As shown in Figure 1B, tumors grew significantly when no drug was administered, while administration of the BPA-uridine conjugate and neutron irradiation effectively inhibited tumor growth. The degree of inhibition was comparable to that of the previously reported BPA-fructose conjugate. These results strongly suggests that BPA-uridine is activated in tumors under irradiation conditions and exerts its cell-killing effect in vivo.

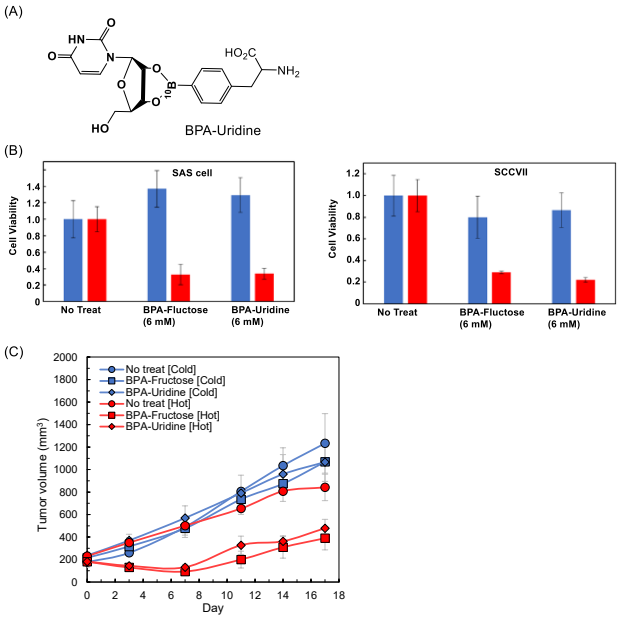

Figure 1. (A) Chemical structure of BPA-Uridine. (B) Cytotoxic effect of BPA-Uridine conjugate upon thermal neutron irradiation (1 MW, 45 min, red: irradiation (+), blue: irradiation (-)) against SAS or SCCVII cells. (C) In vivo evaluation of BPA-uridine or BPA-fluctose as an anticancer agent. Tumor (SAS cells) volumes of each group were measured, epi-/thermal neutrons: 50 min.

REFERENCES:

[1] K. Tanabe *et al.,* Org. Biomol. Chem., **7** (2009) 654.

CO6-5 BPA derivative bearing Hoechst unit for BNCT

K. Tanabe,[1] T. Nishihara,[1] M. Mizutani,[1] and M. Suzuki[2]

[1]*Department of Chemistry and Biological Science, College of Science and Engineering, Aoyama Gakuin University*
[2]*Institute for Integrated Radiation and Nuclear Science, Kyoto University*

INTRODUCTION:

Recently, "Boron Neutron Capture Therapy (BNCT)" has been attracting attention; BNCT is a therapy that selectively damages cancer cells by causing them to accumulate a ^{10}B compound that causes a nuclear reaction with thermal neutrons. However, at present, there are only two types of boron drugs available for BNCT: BPA, a phenylalanine derivative, and BSH, a boron cluster. Therefore, it is an urgent issue to develop drugs for BNCT which show effective therapeutic effects. In this study, we attempted to construct a molecular system to damage genomic DNA by delivering BPA to the cell nucleus. We designed a new boron drug by using Hoechst unit[1] (Hoechst-BPA), which have an ability to be accumulated in the cell nucleus.

EXPERIMENTS:

Neutron capture therapy to SAS tumor models. SAS cells in matrigel (1×10^6 cells per mouse) were subcutaneously inoculated into the right thighs of BALB/c nude mice. The tumors were allowed to grow ~1.5 month. The mouse was injected with fructose-BPA or Hoechst-BPA (250 mg/kg). The mice were placed in acrylic which were secured on a 5-mm-thick thermoplastic plate that contained 40 weight % (wt %) of ^6LiF (96% 6Li) to block thermal neutrons and had a circular hole in the center. The thigh containing the tumor was stretched over the hole, and the tumor was irradiated with epi-/thermal neutrons for 50 min, 1 h after the injection. The tumor size was measured by a caliper, and tumor volume (V) was calculated using the following equation: $V = ab^2/2$, where a and b are the major and minor axes, respectively.

RESULTS:

Last year, we successfully synthesized Hoechst-BPA from a BPA derivative with an azide group and a Hoechst molecule with an alkyne moiety using a cycloaddition reaction called Huisgen reaction.

Initially, the function of Hoechst-BPA was evaluated using cultured cells. A549, human lung cancer cell, was treated with Hoechst-BPA, and then the cells were observed by confocal laser microscopy. As a result, blue fluorescence derived from Hoechst was observed in the cell nucleus. Similar results were obtained when SAS, human squamous cells, and SCC7, mouse squamous cells, were used. These results suggests that Hoechst-BPA was transported into the cell nucleus and bound with genomic DNA.

Next, SAS, and SCC7 cells treated with Hoechst-BPA were irradiated with neutrons and cytotoxic effect was evaluated. We evaluated the cytotoxicity of Hoechst-BPA conjugate against these cells, which were exposed to neutron (1 MW) in the presence of aqueous solution of the conjugate and then incubated at 37 ˚C. Cell survival was determined by WST assay. Hoechst-BPA showed little toxicity without neutron irradiation, but moderate toxicity was observed upon neutron irradiation.

Finally, Hoechst-BPA was administered to tumor-bearing mice (SAS), and then the mice were irradiated with neutrons to evaluate the anti-tumor effect in vivo. One month after irradiation, the tumor volume increased significantly after neutron irradiation to mice without administration of Hoechst-BPA, whereas the increase of tumor volume was greatly suppressed when mice were treated with Hoechst-BPA. Although high cell-killing and antitumor effects were expected, the Hoechst-BPA-treated mice did not show sufficient efficacy. This may be due to insufficient accumulation of Hoechst-BPA in the tumor tissue.

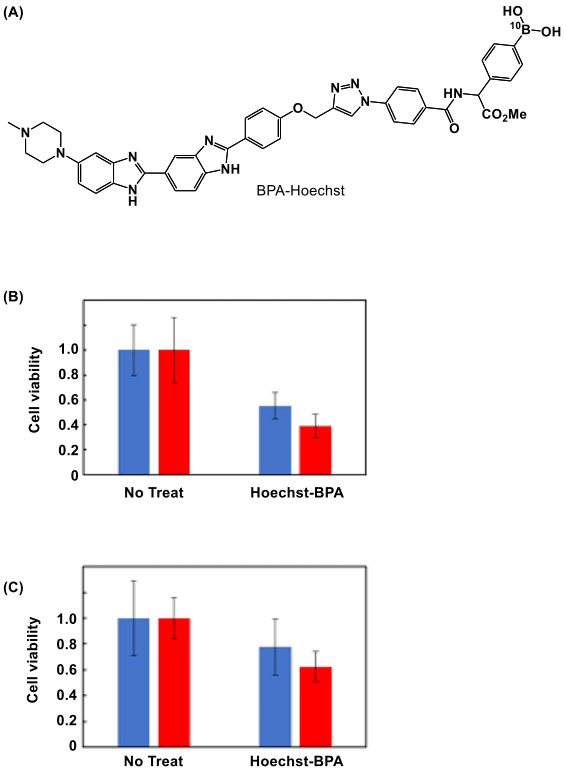

Figure 1. (A) Chemical structure of Hoechst-BPA. (B,C) Cytotoxic effect of BPA-Hoechst conjugate upon thermal neutron irradiation (1 MW, 45 min, red: irradiation (+), blue: irradiation (-)) against SAS (B) or SCCVII cells (C).

REFERENCES:

[1] K. Tanabe *et al.*, ChemBioChem., **19** (2018) 956-962.

CO6-6 Elucidating the Molecular Basis for the Increased Risk of Nuclear Cataract Development with Global Warming

N. Yamamoto[1] and T. Takata[2]

[1] *Fujita Health University*
[2] *Institute for Integrated Radiation and Nuclear Science, Kyoto University*

INTRODUCTION:
The transparency of the lens is important for focusing target onto retina. Maintaining the function of lens determines the quality of life. Lens cells contain rich structural proteins, which is called as crystallin. Those stable long-lived crystallin interactions is critical for lens functions. Many past studies have reported about post-translational modifications in crystallin species decreased solubility of crystallins and lead senile cataract formation in aged lens. Those modifications were accumulated under various stresses during life, such as heat and ultraviolet (UV) irradiation. It has also been considered that many factors in addition to UV are the main causes of nuclear cataract (NUC). In order to elucidate those factors, we performed a worldwide epidemiological survey and confirmed that the risk of NUC is significantly higher in residents living in areas where the annual number of days with temperatures of 30°C or higher is higher. Furthermore, in an *in silico* simulation study, the applicant group showed that the incidence of NUC differs within a range of internal temperature differences (35.0-37.5°C) [1]. These obvious but new results are currently the focus of worldwide attention. Based on these results, this study aims to clarify the relationship between NUC and environmental temperature. We had previously cultured lens model cells in different temperature and analyzed the modification levels of Aspartate (Asp) in crystallin. However, we had not succeeded in mass spectrometry of cell extracts cultured at different temperatures. The reason for this issue would be low amount of target peptides. Therefore, we adopted on membrane digestion and a quadrupole (qqq) mass spectrometry. Those are less comprehensive but with excellent sensitivity to identify the trace modification in peptide.

EXPERIMENTS:
Material Immortalized human lens epithelial cells (iHLEC-NY2) are cultured on different temperature (35.0-37.5°C) and collected by RIPA buffer. All cell extracts were solubilized in the sample buffer for SDS-PAGE, then separated by electrophoresis. Anti-αA crystallin antibody (Santa) was used for western blotting to identify αA-crystallin in cell extracts.
Western Blot and on membrane digestion In order to get intense peptides from isolated αA-crystallin, on membrane digestion was performed. To get a lot of proteins, molar mass of 15,000–30,000 bands from five to seven lanes membrane were collected, then used for on membrane digestion.
LC-MS analysis After trypsin digestion, each tryptic peptide was injected to RP-HPLC-MS/MS (qqq) systems (Shimadzu) to identify the expressed αA-crystallin in iHLEC-NY2. An L-column 2 metal-free (3 μm, 2.0 mm × 150 mm, CERI) was used with the following binary mobile phase compositions: solvent A (0.1% TFA acid aqueous solution) and solvent B (100% acetonitrile containing 0.1% TFA). The algorism for the database search was LabSolutions (Shimadzu) as previously reported [2].

RESULTS:
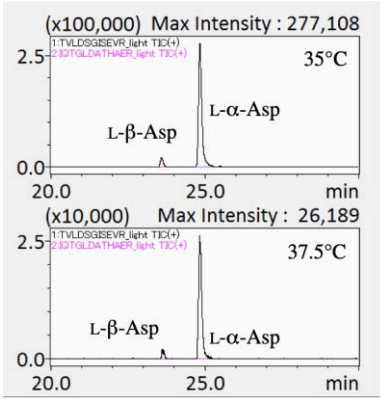

	35°C	37.5°C
Lα	2095229 (94%)	258644 (94%)
Lβ	132898 (6%)	15185 (6%)

Fig. 1. Modifications on Asp58 and Asp151 of αA-crystallin in iHLEC-NY2 extracts.

The conventional LC-MS/MS analysis from tryptic digested cell extracts could not show the peaks, but peptide from on membrane digestion could be observed on RP-HPLC-MS/MS (qqq) systems (Fig. 1). This indicated the significance of current method for identification of trace modification of amino acid residues in proteins. There is a small amount of L-β-Asp 58 in both samples without any differences. The chromatogram of peptide containing Asp151 of αA-crystallin were not observed in both. The amount of sample maybe short for the identification of Asp151, or ionization of peptide was not enough to be observed on current systems. No significant modification was observed at this temperature difference, so the reason of the formation of NUC under high temperature may not be caused by isomerization of Asp58. There were still significant changes in cell proliferation and expression of αA-crystallin, indicating that temperature-dependent changes occur during protein biosynthesis inside the cell. We, therefore, hypothesized that the folding pathways of αA-crystallin and that substrate proteins inside the cell are temperature dependent, and tried to conduct the following study focusing on temperature changes.

REFERENCES:
[1] N. Yamamoto *et al.*, Cells., **12** (2020) 2670.
[2] N. Fujii *et al.*, ACS Omega, **5** (2020) 27626-27632.

CO6-7 Elucidation of the effects of dose rate of radiation on normal and tumor tissues

T. Watanabe[1], Y. Sanada[1], T. Takata[1], G. Edward Sato[2], M. Yoshimura[2], H. Tanaka[1], M. Suzuki[1], T. Mizowaki[2]

[1]*Institute for Integrated Radiation and Nuclear Science, Kyoto University*

[2]*Radiation Oncology and Image-Applied Therapy, Graduate School of Medicine, Kyoto University*

INTRODUCTION: Radiation with different dose rates is known to have different effects on normal tissues [1]. On the other hand, the effect of dose rate on the antitumor effect is minor, and a higher dose rate may improve the therapeutic efficacy ratio of radiation [2]. The purpose of this study is to ascertain whether the dose rate alters the effects of various normal tissues. In addition, experiments were conducted to see if the antitumor effect of radiation could be differentiated by differences in dose rate, which had previously been equivalent, by using drugs that affect the antitumor effect of radiation in combination.

****

EXPERIMENTS: A mouse subcutaneous transplantation model of mouse-derived squamous cell carcinoma cells (SCC7) was used for experiments in C3H mice under the lower limb skin. The differences in the effects of irradiation with electron beams with high dose rates and X-rays with low dose rates on normal and tumor tissues were investigated. The irradiation area was limited to the lower extremities, the remaining area was shielded, and the tumor tissue was irradiated with a single 14 Gy dose. In addition, to evaluate the radiation effects on the skin of one of the normal tissues at different dose rates, the head was irradiated with 14 Gy and the body weight and the states of the irradiated area were observed for one month. Tirapazamine and amifostine were used as agents affecting the antitumor effect of radiation [3, 4]. Tirapazamine and amifostine were each administered 1 hour before irradiation, and tumor tissue was irradiated to confirm tumor size over time.

****

RESULTS: When the upper body of the mice were irradiated, the X-ray group showed significant weight loss up to 12 days after irradiation, whereas the electron beam group, which has a higher dose rate, showed less weight loss and a significant difference. The skin in the irradiated area also showed obvious alopecia and wet desquamation and dermatitis in the X-ray group, whereas the skin in the high-dose-rate electron beam group showed only slight alopecia, no wet desquamation, and no dermatitis. Compared to the X-ray group, the higher dose rate electron beam group showed less redness in the oral cavity and perinasal area. These results suggest that the difference in the degree of weight loss in the two groups was influenced by the severity of oral mucositis. When X-rays were irradiated after preadministration of tirapazamine to subcutaneous tumors in mice, the anti-tumor effect of X-rays was sensitized. Similarly, when the subcutaneous tumors of mice were irradiated with high-dose-rate electron beams after preadministration of tirapazamine, they showed a sensitizing effect of the antitumor effect of X-rays as well. However, the degree of sensitization of the antitumor effect was similar to that of X-ray irradiation, and there was no significant difference in antitumor effect in the combination group of tirapazamine and X-ray irradiation compared to the combination group of tirapazamine and electron beam irradiation. When amifostine was preadministered to mouse subcutaneous tumors followed by X-rays, it showed the same anti-tumor effect as X-rays alone. Similarly, when amifostine was preadministered to subcutaneous tumors of mice and then irradiated with high-dose-rate electron beams, the anti-tumor effect was not attenuated and was similar to that of electron beams alone. However, in this experiment, the degree of sensitization of the antitumor effect was similar to that of X-irradiation, and there was no significant difference in antitumor effect in the combined amifostine and X-irradiation group compared to the combined amifostine and E-beam irradiation group.

****

REFERENCES:

[1] Binwei Lin *et al.,* Front Oncol., **11** (2021) 644400.
[2] Elise Konradsson *et al.,* Advances in Radiation Oncology., **7** (2022) 101011.
[3] B G Siim *et al.,* Cancer Res., **57** (1997) 2922-8.
[4] Jr William Small *et al.,* Int. J. Gyn. Can., **21** (2011) 1266-75.

R4041

CO6-8 Asp racemization/isomerization in shedding products of cell adhesion molecule 1 is potentially involved in the neurodegeneration induced by elevated pressure

A. Yoneshige[1], A. Ito[1] and T. Takata[2]

[1]*Department of Pathology, Kindai University*
[2]*Institute for Integrated Radiation and Nuclear Science, Kyoto University*

INTRODUCTION: The elevation of internal pressure is often involved in neurodegeneration; intraocular and intraventricular pressure elevations over 20–30 cmH_2O cause glaucoma and hydrocephalus, respectively.
Previously, to investigate the mechanisms by which elevation of intraluminal pressure causes cell or tissue degeneration, we devised a novel two-chamber culture system that enabled us to subject cultured cells to low levels of water pressure (2-50 cmH_2O pressure load) [1,2]. We found that mouse primary neurons degenerated when the water pressure was above 30 cmH_2O, and that ectodomain shedding of synaptic cell adhesion molecule 1 (CADM1) increased in a water pressure-dependent manner [1]. We also discovered that the increase of intracellular product of CADM1 shedding (C-terminal fragment, CADM1-CTF) resulted in decreased neurite density with punctate localization of CADM1 suggesting its aggregation in neurites [1].
CADM1-CTF is rich in Asp residues neighbored by Ala residues, and the conversion of these amino acids to poly-Gly diminished its aggregation state. Since the racemization and isomerization of Asp residues contributes to aggregation of various proteins and it likely occurred when the neighboring residues are small [3,4], these insights led us to hypothesize an involvement of Asp racemization/isomerization in the neurodegeneration induced by internal pressure elevation.

EXPERIMENTS:
(1) Synthetic peptide of internal sequence of CADM1-CTF (GADDAADADTAIINAEGGQNNSEEK) was incubated at 50°C for 0-15 days and applied to LC-MS to identify Asp isomer-containing peptides.
(2) Mouse neuroblastoma cell line Neuro-2a cells with exogenously expressed CADM1-CTF were cultured under 50 cmH_2O and were prepared for LC-MS analysis.
(3) To mimic oxidative stress induced by internal pressure elevation, Neuro-2a cells expressing CADM1-CTF were treated with hydrogen peroxide and the cells were subjected to the isolation of CADM1-CTF by immunoprecipitation.

RESULTS:
(1) In LC-MS analysis of CADM1-CTF synthetic peptide, multiple peaks were detected after 1 day at pH 6.0 or pH 7.0 indicating that Asp racemization/isomerization could occurred under neutral pH.
(2) CADM1-CTF proteins in Neuro-2a cells were solubilized with water, Triton X-100 containing buffer, or SDS containing buffer after 3 days culture under 50 cmH_2O, and CADM1 immunoblot was carried out. CADM1-CTF protein yields (CADM1-CTF / total proteins) were in the order Triton X-100 > SDS > water, however, the peptide peak was not identified using with LC-MS.
(3) Previously, we found that CADM1 shedding was increased by oxidative stress as a cause of pulmonary emphysema in cigarette smoke exposure [5]. We furthermore showed that Lipocalin-2, an iron binding protein was upregulated in the retinae under 50 cmH_2O pressure [6]. Since iron dysregulation induces oxidative stress, we decided to explore the linkage between oxidative stress and Asp racemization/isomerization of CADM1-CTF. Our preliminary data demonstrated that CADM1-CTFs could isolate from Neuro-2a extracts by immunoprecipitation (Fig.1). Future experiments are planned for identification of Asp isomer by LC-MS or anti-D-Asp antibody (if available) in these immunoprecipitated CADM1-CTFs.

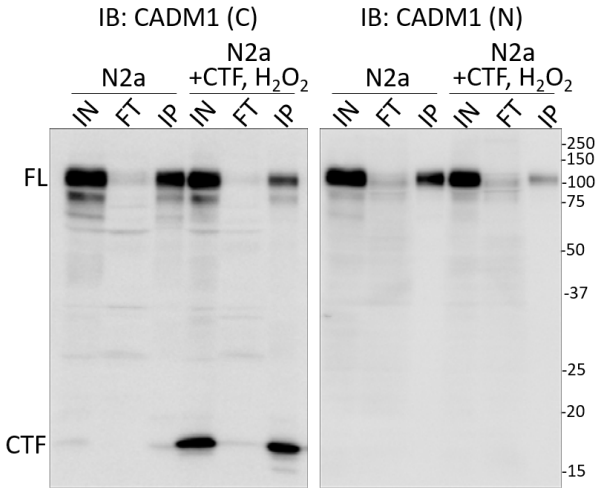

Fig. 1. Isolation of CADM1-CTFs from Neuro-2a (N2a) cell lysate by immunoprecipitation. Full length (FL)-CADM1 and CADM1-CTFs were isolated with antibody recognizing CADM1 C-terminal peptide and detected by immunoblotting (IB) with anti-CADM1 C-terminus (C) or anti-CADM1 N-terminus (N) antibody respectively. IN: input, FT: flow-through, IP: immunoprecipitated sample.

REFERENCES:
[1] A. Yoneshige *et al.*, Mol. Neurobiol., **54** (2017) 6378-6390.
[2] M. Hagiyama *et al.*, Front. Physiol., **8** (2017) 997.
[3] N. Fujii *et al.*, J. Biochem., **116** (1994) 663-669.
[4] T. Takata *et al.*, Protein Sci., **29** (2020) 955-965.
[5] A. Ri *et al.*, Front. Cell Dev. Biol., **6** (2018) 52.
[6] A. Yoneshige *et al.*, Front. Cell Dev. Biol., **9** (2021) 664327.

CO6-9 SAXS analysis for elucidating the inhibitory mechanism of the amyloid precursor of insulin B-chain through the interaction with αB-crystallin

Y. Kokuo, K. Yuzu, N. Yamamoto[1], K. Morishima[2], A. Okuda[2], R. Inoue[2], M. Sugiyama[2], J. Hayashi[3], J. A. Carver[3], E. Chatani

Graduate School of Science, Kobe University
[1]*Graduate School of Medicine, Jichi Medical University*
[2]*Institute for Integrated Radiation and Nuclear Science, Kyoto University*
[3]*Research School of Chemistry, The Australian National University*

INTRODUCTION: Amyloid fibrils are protein aggregates showing fibrous morphology and β-sheet-rich inner structure, and they are deeply involved with amyloidoses and neurodegenerative diseases. A cellular strategy for preventing the formation of amyloid fibrils is the expression of small heat shock proteins (sHsps), which have been proposed to rescue unfolded protein in an ATP-independent manner. αB-crystallin (αB-C) is a typical member of sHsps in mammals, and there have been reported its inhibitory effects against amyloid formation in vitro. However, the mechanism of the inhibition remains to be fully elucidated.

In this study, we analyzed the mechanism by which αB-C inhibits fibrillation by using insulin B-chain (B-chain) as a substrate. B-chain is an excellent model of amyloidogenic proteins, as it forms amyloid precursors prior to αB-C amyloid nucleation [1-4]. We previously found that αB-C inhibit the B-chain fibrillation through interacting with the B-chain amyloid precursors [5], and here, we performed small-angle X-ray scattering (SAXS) in combination with analytical ultracentrifugation (AUC) measurements to clarify the change in size and shape of the amyloid precursor formed under reactions in the presence of αB-C.

EXPERIMENTS: Insulin B-chain was dissolved at a final concentration of 400 μM in 50 mM Tris-HCl buffer (pH8.7) containing 5 mM NaCl and αB-C at the molar ratio ranging from 0 to 0.2. After overnight incubation at 25 °C, the samples were subjected to SAXS measurements. A SAXS profile was collected at 25 °C and 30-minute exposure with a NANOPIX equipped with a HyPix-6000 (Rigaku Corporation, Japan). A Cu K-α line (MicroMAX-007HFMR) was used as a beam source, which was further focused and collimated with a confocal multilayer mirror (OptiSAXS). The camera length was set to 1.33 nm and the range of the scattering vector q was from 0.008 to 0.20 Å^{-1}.

AUC was conducted with a ProteomeLab XL-I analytical ultracentrifuge (Beckman Coulter, USA) to analyze the weight distribution of the B-chain/αB-C complex and unbound αB-C. Sedimentation velocity analytical ultracentrifugation (SV-AUC) measurements were performed using Rayleigh interference optics at 40,000 rpm at 25 °C with a 1.2 mm path-length cell. The experimental data were analyzed with SEDFIT software. The density and viscosity of solvent, and partial specific volume of each protein was calculated from its amino acid sequence with SEDNTERP software.

RESULTS: The SAXS profiles of the B-chain-αB-C complex formed at five different molar ratios (1:0, 1:0.025, 1:0.05, 1:0.1, and 1:0.2) are shown in Fig. 1A. It was found from the AUC analysis that αB-C became excess at a higher molar ratio, and therefore, the fraction of unreacted αB-C was subtracted from the SAXS profile to obtain the profiles of the B-chain-αB-C complex selectively. The slope of the log-log plot was close to −1 for all samples, suggesting that the complex has a rod-like morphology like the B-chain amyloid precursor. To calculate the base diameter of the complex, the cross-section plot was constructed in Fig. 1B. The slope of this plot became steeper at higher molar ratio, suggesting that the complexes tend to become thicker as the concentration of αB-C increased. Although the length was difficult to be estimated from the SAXS profile because of limited Q range, the hydrodynamic diameter from dynamic light scattering has suggested that the complex tended to become shorter upon increasing the αB-C concentration.

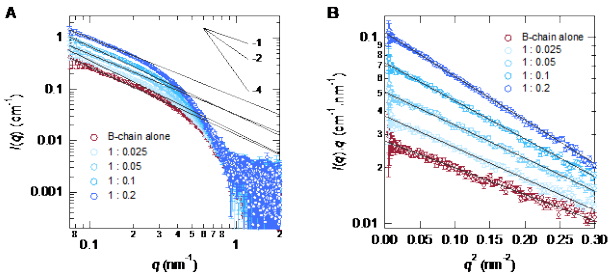

Fig. 1. (A) SAXS profiles and (B) their cross-section plots of the B-chain-αB-C complexes formed at different molar ratios of B-chain:αB-C. In this figure, unreacted αB-C is already subtracted to show the SAXS profiles of the B-chain-αB-C complexes themselves. The profile of the B-chain amyloid precursor, which is formed by B-chain alone, is also shown as a reference. The slopes in (A) in the intermediate region suggest that the complexes have a rod-like shape, and from the slopes in (B), the base diameters of the rod-like complexes have been estimated.

REFERENCES:

[1] N. Yamamoto *et al.*, Sci. Rep., **8** (2018) 62.
[2] N. Yamamoto *et al.*, Biochemistry, **58** (2019) 2769-2781.
[3] Y. Yoshikawa *et al.*, Molecules, **27** (2022) 3964.
[4] N. Yamamoto *et al.*, J. Phys. Chem. B, **126** (2022) 10797-10812.
[5] Y. Kokuo, Master Thesis, Kobe Univ. (2023).

CO6-10 Detection of the LIM Kinase 1 and Fam81a multimeric complex

T. Saneyoshi[1], T. Hirouchi[1], T. Kaizuka[2,3], A. Okuda[4], K. Morishima[4], T. Takumi[3], M. Sugiyama[4], Y. Hayashi[1]

[1] *Graduate School of Medicine, Kyoto University*
[2] *Centre for Clinical Brain Sciences, University of Edinburgh*
[3] *Graduate School of Medicine, Kobe University*
[4] *Institute for Integrated Radiation and Nuclear Science, Kyoto University*

INTRODUCTION: LIM kinase 1 (LIMK1) is a kinase involved in actin cytoskeletal regulation by phosphorylating actin binding protein cofilin. In neurons, it is involved in structural plasticity of dendritic spines. LIMK1 has been shown to dimerize upon activation but not further details are known as to its high order structure [3]. On the other hand, FAM81A is a postsynaptic density (PSD) localized protein containing coiled-coil structure [1]. We have demonstrated that recombinant mouse Fam81a undergoes liquid-liquid phase separation, interacts with PSD proteins, including PSD-95, SynGAP, and NMDA receptors, and promotes condensation of those proteins [2]. However, no further characterization has been reported about Fam81a, neither.

We therefore investigated whether recombinant mouse LIMK1 and Fam81a forms multimeric complex or not by performing dynamic light scattering (DLS) and analytical ultracentrifugation (AUC) to detect a multimeric complex of Fam81a and estimated its molecular size.

EXPERIMENTS: Full length LIMK1 fused with GST was purified from baculovirus expression system using Sf9 cells. Fam81a were produced as a GST-fused form in an *E.coli* expression system. The GST-fusion proteins were pulled down using glutathione agarose beads. After cleaving GST tag using HRV3C protease, the target protein was purified by size exclusion chromatography using HiLoad 16/600 superdex 6 pg. The purify of the proteins were assessed by CBB staining of SDS-PAGE.

RESULTS: We successfully purified both recombinant proteins. They were then examined by DLS and AUC and their oligomerization status was determined. We plan to confirm the results further by cryoEM. The LIMK1 structure will be used to design FRET probe to detect its conformational change that may represent activity. The result will be published in scientific journal.

REFERENCES:

[1] R. Li *et al.,* FASEB J., **20** (2006) 1218-1220.
[2] A. Dosemeci *et al.*, Neurosci. Lett., **699** (2019) 122-126.
[3] T. Kaizuka *et al.*, bioRxiv, (2023).
(doi) 10.1101/2023.01.23.525126.

CO6-11 Structural Analysis of Ceramide Transport Protein (CERT)

S. Morita[1], K. Morishima[2], T. Fujita[1], N. Sato[2], A. Okuda[2], K. Hanada[3], M. Sugiyama[2] and C. Kojima[1,4]

[1]*Graduate School of Engineering Science, Yokohama National University*
[2]*Institute for Integrated Radiation and Nuclear Science, Kyoto University*
[3]*National Institute of Infectious Diseases*
[4]*Institute for Protein Research, Osaka University*

INTRODUCTION: Lipids are important components of cell membranes. Lipids are synthesized in the endoplasmic reticulum and transported to the Golgi apparatus, where they are chemically modified. Lipid transfer proteins (LTPs) are known to transport lipids from the endoplasmic reticulum (ER) to the Golgi apparatus. Ceramide is one of the lipids and is transported by ceramide transfer protein (CERT). CERT consists of three segments, a PH domain that interacts with PI4P and contributes to Golgi localization, a START domain that binds to ceramide, and a middle region (MR) connecting the PH and START domains [1]. The MR is known to contain functional sites such as the FFAT motif that interacts with the ER membrane protein VAP and the serine repeat motif (SRM) that inhibits ceramide transport by phosphorylation. Among these regions, the structures of the PH and START domains have already been determined, but neither the MR nor full-length structures of CERT have yet been analyzed. Here the structural analysis of the full-length CERT was performed with the aim of elucidating the mechanism of ceramide transport mediated by CERT.

EXPERIMENTS: The wild-type and dominant-negative mutant samples of the full-length CERT were expressed using *E. coli* and purified by affinity chromatography and gel filtration chromatography. The samples were analyzed by gel filtration chromatography. The dominant-negative mutant was further analyzed by MS spectrum, analytical ultracentrifuge, and small-angle x-ray scattering.

RESULTS: Both the wild-type and dominant-negative mutant samples of the full-length CERT were successfully expressed and purified. The sample purity was evaluated by SDS-PAGE as a single band. Both samples were analyzed by the gel filtration chromatography. The apparent molecular mass evaluated from the elution volume of the gel filtration chromatography (Fig. 1) was 215 and 254 kDa for the wild-type and dominant-negative mutant samples of the full-length CERT, respectively, and close to that of the CERT trimer, 204 kDa. In the cells, the full-length CERT is reported to form a trimer [2]. The elution volume of the gel filtration chromatography depends on both molecular weight and shape. Therefore, we assumed that both samples are trimer with different molecular shapes and that molecular shape of the dominant-negative mutant sample is distorted.
To investigate this assumption, the molecular mass and shape of the dominant-negative mutant sample of the full-length CERT were evaluated by the analytical ultracentrifuge (Fig. 2). Assuming the ratio of the friction coefficients f/f_0 = 1.8, the major sedimentation coefficient for the dominant-negative mutant sample was found as 7.2 S ~ 212 kDa which is close to that of the CERT trimer, 204 kDa. The f/f_0 value 1.8 indicates the molecular shape is significantly distorted with the axial ratio ~ 12. The observed molecular mass and distorted shape of the dominant-negative mutant sample are consistent with our assumption based on the gel filtration analysis.

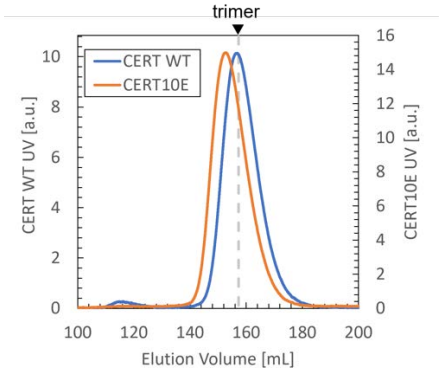

Fig. 1. The gel filtration chromatography of the wild-type (blue) and dominant-negative mutant (orange) samples of the full-length CERT. The down-closed black triangle on the top shows the elution volume of the 204 kDa protein which is the molecular mass of the CERT trimer.

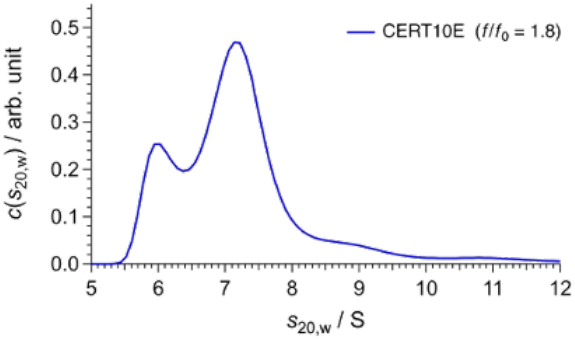

Fig. 2. The distribution function of the sedimentation coefficient obtained from the c(s) analysis of the analytical ultracentrifuge measurement for the dominant-negative mutant of the full-length CERT.

REFERENCES:
[1] K. Kumagai and K. Hanada, FEBS Lett., **593** (2019) 2366-2377 .
[2] A. Goto *et al.,* Int. J. Mol. Sci., **23** (2022) 8576.

CO6-12 Small-angle X-ray Scattering toward Understanding Chromosomal Modulation by Topoisomerases

M. Shimizu, A. Okuda, Y. Yunoki, R. Inoue, K. Morishima, N. Sato, R. Urade, and M. Sugiyama

Institute for Integrated Radiation and Nuclear Science, Kyoto University

INTRODUCTION: In both eukaryotes and prokaryotes, functions of chromosomes have a strong relationship with superhelicity of the genomic DNA. During the DNA transcription and DNA replication, complexed protein machines proceed on the genomic DNA while unwinding the DNA duplexes. These processes accumulate positive superhelicity in the direction of the molecular machines, and accumulate negative superhelicity in the opposite direction [1, 2]. As a result, progression of the complex becomes more difficult. Therefore, mechanisms are needed to control the level of superhelix and to maintain the progression of the molecular machines [3]. Conversely, DNA superhelix are also known to promote formation of a certain complexes [4]. This can be interpreted as stabilization of curved DNA structure promotes the formation of a protein complex that form across two DNA regions or that form at a DNA loop. In other words, cells sometimes deal with the DNA superhelix as an obstacle to be overcome, and at other times they utilize it. With this background, it is critical to maintain the superhelical level of the genomic DNA. DNA topoisomerases are responsible for maintaining the DNA superhelicity. There are two major types of DNA topoisomerase, type I and type II. The type I topoisomerases break covalent bond of one strand of the DNA duplex, and then restore the DNA chain after their superhelical level has changed. The type II topoisomerases cleave both DNA strands, introduce superhelicity, and restore the DNA strands [5]. The detailed process by which DNA superhelicity introduced by topoisomerases spreads over a wide area of the genomic DNA and affects transcription and replication is not yet clear. The dynamic process cannot be captured by X-ray crystallography or cryo-electron microscopy. Single-molecule measurements have studied the global conformational changes in DNA exerted by DNA topoisomerases [6, 7]. However, chromosomes in cells are more complex systems in which many factors interact. Therefore, we focused on small-angle X-ray scattering measurements, which provides information on structural ensemble of biomolecules, to study topoisomerase-induced changes in huge DNA-protein complexes. As the first step to achieve this, we examined a condition for measuring long double stranded DNA with small-angle X-ray scattering system in the Institute for Integrated Radiation and Nuclear Science, Kyoto University.

EXPERIMENTS: SAXS measurements were performed on the pUC19 linearized vector supplied with the In-Fusion HD Cloning Kit (Takara Bio USA, Inc., CA, USA, Clontech Laboratories, Inc., CA, USA). After replacing the DNA-dissolving buffer by dialysis, small-angle X-ray scattering measurements were performed for 6 hours.

RESULTS: In small-angle scattering, the scattering intensity near zero scattering vector is proportional to the square of the molecular weight of the sample. We tried to measure plasmid DNA at low concentrations because we expected that the large molecular weight would guarantee sufficient scattering intensity even at low concentrations. After replacement of buffer by dialysis, the sample concentration was 22.9 μg/mL. The radius of gyration from the SAXS profile was 36.11 ± 1.54 Å. In order to identify the structural ensemble of this DNA, it is necessary to design measurements with smaller measurement errors. In summary, the results suggest that a sample concentration of about 1 mg/mL is required even when measuring large DNA systems.

REFERENCES:

[1] L. F. Liu and J. C. Wang, Proc. Natl. Acad. Sci. USA, **84(20)** (1987) 7024-7027.

[2] L. Postow *et al.,* Proc. Natl. Acad. Sci. USA, **98(15)** (2001) 8219-8226.

[3] S. J. McKie *et al.,* BioEssays, **43(4)** (2021) 2000286.

[4] K. Kasho *et al.,* J. Biol. Chem., **292(4)** (2017) 1251-1266.

[5] J. J. Champoux, Annu. Rev. Biochem., **70** (2001) 369-413.

[6] A. Basu *et al.,* Nat. Chem. Biol., **14(6)** (2018) 565-574.

[7] D. Spakman *et al.,* Nucleic Acids Res., **49(10)** (2021) 5470-5492.

CO6-13 Character of DNA damage induced by nuclear palnt neutron beams

H. Terato, T. Hanafusa, M. Isobe, Y. Sakurai[2], and T. Saito[2]

Advanced Science Research Center, Okayama University
[1]Graduate School of Medicine, Dentistry, and Pharmceutical Sciences, Okayama University
[2]KURNS

INTRODUCTION: DNA is a main target of radiation biological effects. This is because DNA is the only molecule responsible for genetic information, and when it is broken, the life events corresponding to the broken part are stalled. This breakdown of DNA is called DNA damage, as a radiation DNA damage. Radiation DNA damage are generated by direct and indirect effects of ionizing radiation. In the former process, ionizing radiation attack and ionize DNA directly. In the latter process, ionizing radiation react water molecules, which are abundant in the organism, and various reactive oxygen species (ROS) are generated. These ROS cause oxidative damage to DNA. For oxidative DNA damage, especially oxidative base damage, the sites of ROS attack have been largely identified in the DNA molecule, and both their types and yields are fairly accurate by previous studies. In the early days of radiation research, such studies were conducted with readily available X-rays and gamma rays, but now they are conducted with a variety of radiation types, including particle beams. It has been found that the type and yield of DNA damage varies greatly depending on the wire type. We have studied for the DNA damage with heavy ion beams, previously [1, 2]. These studies indicated that the DNA damage with heavy ion beams were unique, indicating that a lot of clustered DNA damage were generated including DNA double strand break (DSB), and clustered base lesions. Clustered DNA damage is a complex damage containing multiple lesions in the local region of DNA. This damage is mainly produced by highly concentrated ROS produced by heavy ion beam. This complexed damage can inhibit DNA polymerization with high efficiently stopping of DNA polymerase moving on DNA, and this damage shows less repairable.

Neutron beam shows severe biological damage like heavy ion beams, but its elucidation is still in the middle of research. In this study, we analyze the DNA damage with neutrons from nuclear power plant to unveil the molecular mechanism of biological effect with neutron beam. In the previous study periods, we found the relatively higher yields of DNA damage with the neutron beams than gamma-rays. In this fiscal year of the research project, we conducted irradiation experiments using several DNA repair-deficient strains to determine what DNA damage species are specific to neutron radiation.

EXPERIMENTS: Cultured cells of Chinese hamster ovary (CHO) strains with various DNA repair background were irradiated with neutron beams in the Kyoto University Reactor. The cells were cultivated with the conventional method. The logarithmic growing cells were recovered by trypsinization and set into polypropylene tubes for irradiation. The estimated dose rate of neutron was 1 Gy h^{-1}. The irradiation periods were 0, 30, 60, 90, 120, 150 min. The irradiated cells were divided into two groups, one for viability and the other for DNA damage analysis. For viability, the cells were immediately dissolved again with the cultured medium and reseeded into fresh medium. The cells were cultivated for 10 days for growing the colony. The colony was fixed with ethanol and stained with methylene blue. The colony number was counted for estimation of the irradiated cell viability. Simultaneously a half of the sampled cells were analyzed by agarose gel electrophoresis for DNA damage estimation. For DNA damage analysis, the irradiated cells were immediately frozen and stored at -80°C until the analysis. The frozen cells were embedded in low melting agarose plug and treated by protease. Then the plugs were subjected by electrophoresis in the manner already reported [2]. We use the Kindai reactor in parallel to conduct our research. This is to generalize the results from the various reactors.

RESULTS AND DISCUSSION: There were a variety of DNA repair-deficient strains of CHO used in this study, but only one is reported here for reasons of space. CHO-V3 strain is deficient in DNA-PK_{cs}, which prevents the function of nonhomologous end joining (NHEJ). Thus, it is extremely susceptible to DNA double-strand breaks, the major DNA damage caused by radiation. The degree of sensitivity with D_{37} of CHO-V3 for the neutron beam was 0.22 Gy. On the other hand, the D_{37} of CHO-AA8, a wild type of CHO-V3 was 0.39 Gy. Its sensitivity to neutron radiation is ten times higher than that of gamma radiation. And NHEJ insufficiency increases that sensitivity by a factor of two. Its sensitivity to neutron radiation is ten times higher than that of gamma radiation. And NHEJ insufficiency increases that sensitivity by a factor of two. This means that neutrons produce DSBs, which are the target of NHEJ repair. However, the increase in susceptibility is only 2-fold, which may indicate that the susceptibility is already high enough, or that some other damage species other than DSBs are produced by neutrons. The contribution of gamma-rays contaminated in the reactor neutron beams must also be clarified. We will await the results of the DNA damage analysis we are going to perform and discuss.

REFERENCES:

[1] H. Terato *et al.,* J. Radiat. Res., **49** (2008) 133-146.
[2] Y. Tokuyama *et al.,* J. Radiat. Res., **56** (2015) 446-455.

CO6-14 Distribution analysis of the chemical modification of the amino acid residues in mice lens structural proteins during age-related cataract

S. Matsushita[1], A. Nakamura[1], Y. Suzuki[1] and T. Takata[2]

[1] *Dept of Materials and Applied Chemistry, Nihon University*
[2] *Institute for Integrated Radiation and Nuclear Science, Kyoto University*

INTRODUCTION:
Age-related cataracts are the leading causes of blindness in world. Several risk factors, contributing to the development of cataracts, have been reported. Above all, abnormal lens protein aggregation and insolubilization has been believed as the main process [1]. Alteration of lens protein structure, caused by covalently post-translational modifications, are thought to be critical for maintaining lens protein homeostasis. We have shown that the isomerization of Aspartate residues (iso-Asp) as a scale for a lens aging. One of those Asp is Asp151 in human lens αA-crystallin. Since the sequence of αA-crystallin was highly conserved in mammal, we also used the same method to identify the isomerization of Asp151 in porcine lens previously. As a result, we could identify the isomerization of Asp151 in adult porcine lens. However, the distribution of iso-Asp151 in lens was very obscured. Therefore, we are to address revealing the distribution of isomerized Asp containing proteins in the lens.

Imaging Mass Spectrometry (IMS) is a powerful tool for revealing the distribution of biomolecules, including proteins, on tissues. This technique requires the preparation of high-quality sections. However, it is difficult to prepare sections from water-rich tissue, such as lens. In addition, sensitivity is decreased by background peaks and ionization efficiency. Therefore, it is essential for optimizing sample preparation to analyze the target molecules/modifications.

We have tried different methods to establish the high-quality section of lens. In this study, we first attempted to contain the tissue block with 4% carboxyl methylcellulose (CMC) for preparing lens sections. Next, we attempted to sealed small biomolecules on lens by metal nanoparticles of Zinc Oxide (ZnO) and compared them with cataract and aged eyes [2].

EXPERIMENTS:
ZnO solution
ZnO was suspended in 40 mM sodium acetic acid in acetonitrile/water/trifluoroacetic acid (50/50/0.1, v/v/v) at a concentration of 1 mg/mL.
Tissue section
The cataractous and control lensed were collected from C57BL/6JJcl female mice (CLEA Japan, Inc.,). After extraction of lenses, there lensed were frozen immediately without fixation. The eyes were embedded in 4% CMC solution in liquid nitrogen, following to be sectioned into 10 μm thicknesses, then put on the indium-thin-oxide-coated glasses. The sections were coated with ZnO solution using a manual sprayer.
IMS
A JMS-S3000 SpiralTOF-MS system (JEOL) was used in the spiral-positive ion mode with a detection range of *m/z* 100-1000 for IMS.

RESULTS:
Unfortunately, huge cracks were observed in sections, even if those were embedded by CMC. We tried to use higher concentration of CMC, yet there were still occurring cracks on the lens. The CMC was easily peeled while spraying the ZnO solution, would cause the loss of sections on preparation. Therefore, we must do effort to optimize sample preparation/spraying methods for obtaining ideal images for IMS.

In current study, we found out some small biomolecules in each eye sample. In comparison of signal intensities, we found molecule, being *m/z* 103.9 from cataract tissue, was higher than that from aged eyes (Fig. 1). Distribution of the peak were located on the scleral on control aged lens, but not intense on cataract lens. To the end, we success to show difference of small molecule distribution even in clacked lens section between aged and cataractous lenses, but still need to be optimizing methodology for getting distribution of peptides in further study.

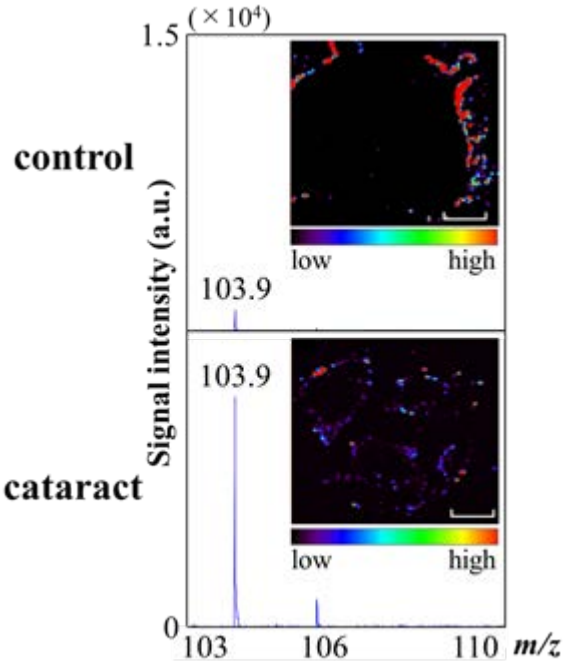

Fig. 1. MS spectra of each sample and distribution at *m/z* 103.9. (Scale bar: 0.5 mm).

REFERENCES:
[1] N. Fujii *et al.*, Biochim. Biophys. Acta, **1860** (2016) 183-191.
[2] C. Chen *et al.,* J. Am. Soc. Mass. Spectrom., **32** (2021) 1065-1079.

CO6-15 Neutron activation of medicines for development of new imaging methodology

A. Toyoshima, N. Koshikawa[1], Y. Kadonaga[2], M. Masubuchi[1], S. Takahashi[1], K. Tokoi[3], H. Aoto[4] and J. Kataoka[1]

Institute for Radiation Sciences, Osaka University
[1]Graduate School of Advanced Science and Engineering, Waseda University
[2]Graduate School of Medicine, Osaka University
[3]Graduate School of Science, Osaka University
[4]School of Science, Osaka University

INTRODUCTION: In the drug delivery system, it is desired to obtain high therapeutic effects with no side-effects by direct transportation of medicine to lesion. At present, it is impossible to simultaneously evaluate the accumulation of administrated medicine in a targeted organ and its therapeutic effect without incision. Imaging of radiations emitted from activated medicine, however, makes it possible to visualize the pharmacokinetics without incision. In our group, an advanced imaging camera available for a wide energy range of X- and γ-rays has been already developed [1]. Previously, we reported the activation of gold nano-particle (AuNP), platinum nano-particle (PtNP), Cisplatin, and Gadoteridol by thermal neutron to produce short-lived radioisotopes suitable for imaging: ^{198}Au (half-life = 2.69 d), ^{159}Gd (18.48 h), and ^{197}Pt (18.3 h) [2]. In this study, we investigated preparation and stability of activated AuNP and Cisplatin for developing a novel methodology of the radioactivated medicine imaging. In addition, we performed the visualization of activated AuNP.

EXPERIMENTS: Dried mPEG-modified gold nano-particles (AuNP-S-mPEG) in polypropylene (PP) tubes were enclosed in small plastic bags. Cisplatin was also enclosed in a small plastic bag. The prepared AuNP and Cisplatin samples were irradiated by neutron using the Pn-2 pneumatic transport system of KUR for 10 min at 5 MW. After the irradiation, these were transported to Osaka University. [^{198}Au]AuNP-S-mPEG was dissolved in deionized water. Condition of [^{198}Au]AuNP-S-mPEG was investigated by ultraviolet-visible absorption spectroscopy (UV-vis). After that, we performed imaging of the [^{198}Au]AuNP-S-mPEG with hybrid Compton camera (HCC) which can visualize wide-band X-rays and gamma rays ranging from a few tens of keV to nearly 1 MeV. The [^{198}Au]AuNP-S-mPEG sample was added into three holes with 10-mm diameters on a phantom. HCC was placed 2 cm apart from the phantom, and measurement with HCC was performed for 20 min. The energy window was set to 412±30 keV to visualize the 412-keV gamma ray emitted form Au-198. As for cisplatin, the stability of activated samples was investigated using high-purity liquid chromatography (HPLC).

RESULTS: Irradiation of neutron in KUR gave approximately 0.4 MBq of [^{198}Au]AuNP-S-mPEG, which contains 25 μg of Au. Photos of dried AuNP before irradiation and dissolved AuNP after irradiation are shown in Figs. 1 (a) and (b), respectively. The red color of the dissolved AuNP suggests that no critical aggregation occurred even after the irradiation. Obtained UV-vis Spectra are shown in Fig. 1 (c). The blue, green, and red and purple lines represent non-irradiated (cold) AuNP dissolved in deionized water, cold AuNP which was dried in PP tube and then re-dissolved in deionized water, AuNP irradiated with neutrons and then dissolved in deionized water. Peaks around 510 nm originated from AuNP. Comparing the blue/green lines (AuNP before irradiation) and red/purple lines (AuNP after irradiation), no significant peak shift was observed. This confirms that the AuNP were successfully activated without aggregation under the present condition. It should be noted that the aggregation was observed under some other irradiation conditions using the different types of AuNP or PP tubes. Therefore, further investigation is necessary to determine the optimum conditions.

The image of [^{198}Au]AuNP-S-mPEG in the three 10-mm holes on the phantom is shown in Fig. 2. The 3 holes were clearly separated, which suggests the potential of HCC as the effective device to visualize the accumulation of the AuNP in organs of a mouse.

In the results of HPLC of cisplatin, hydrolysis of Pt bonds was partly observed. This denaturation of cisplatin is under investigation; there are some possible causes other than neutron irradiation such as photolysis. We will clarify the reason of denaturation and establish the optimum method to generate radioactive cisplatin.

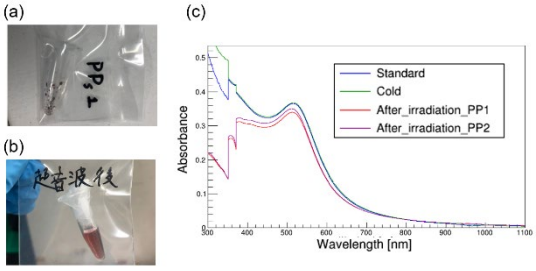

Fig.1. (a) Dried AuNP in PP tube, (b) dissolved AuNP in deionized water after neutron-irradiation, and (c) Result of UV-vis.

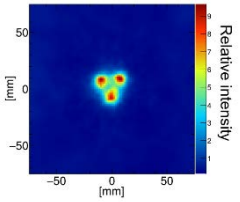

Fig. 2. Image of activated AuNP obtained with HCC.

REFERENCES:

[1] A. Omata *et al.*, Sci. Reports, **10** (2020) 14604.
[2] N. Koshikawa *et al.*, Nucl. Instrum. Methods Phys. Res. A, **1045** (2023) 167599.

CO6-16 Polyglycerol Functionalized ^{10}B Enriched Boron Carbide Nanoparticle as an Effective Bimodal Anticancer Nanosensitizer for Boron Neutron Capture and Photothermal Therapies

Y. Wang[1], G. Reina[1], H. G. Kang[1], X. Chen[1], Y. Ishikawa[2], M. Suzuki[3], and N. Komatsu[1]

[1] *Graduate School of Human and Environmental Studies, Kyoto University*
[2] *National Institute of Advanced Industrial Science and Technology, Research Institute for Advanced Electronics and Photonics, Central 5, 1-1-1 Higashi, Tsukuba, Ibaraki 305-8565*
[3] *Institute for Integrated Radiation and Nuclear Science, Kyoto University*

Boron neutron capture therapy (BNCT) is a non-invasive cancer treatment with little adverse effect utilizing nuclear fission of ^{10}B upon neutron irradiation [1]. While neutron source has been developed from a nuclear reactor to a compact accelerator, only two kinds of drugs, boronophenylalanine and sodium borocaptate, have been clinically used for decades despite their low tumor specificity and/or retentivity. To overcome these challenges, various boron-containing nanomaterials, or "nanosensitizers", have been designed based on micelles, (bio)polymers and inorganic nanoparticles. Among them, inorganic nanoparticles such as boron carbide can include much higher ^{10}B content, but successful *in vivo* applications are very limited. Additionally, recent reports on photothermal effect of boron carbide motivated us to add another modality of photothermal therapy. In this study, ^{10}B enriched boron carbide ($^{10}B_4C$) nanoparticle was functionalized with polyglycerol (PG), giving $^{10}B_4C$-PG with enough dispersibility in a physiological environment [2]. Pharmacokinetic experiments show that $^{10}B_4C$-PG fulfills the following three requirements for BNCT; 1) low intrinsic toxicity, 2) ^{10}B in tumor / tumor tissue (wt/wt) ≥ 20 ppm and 3) ^{10}B concentrations in tumor / blood ≥ 3. *In vivo* study reveals that neutron irradiation after intravenous administration of $^{10}B_4C$-PG suppressed cancer growth significantly and eradicated cancer with help of near-infrared light irradiation (Fig. 1) [3].

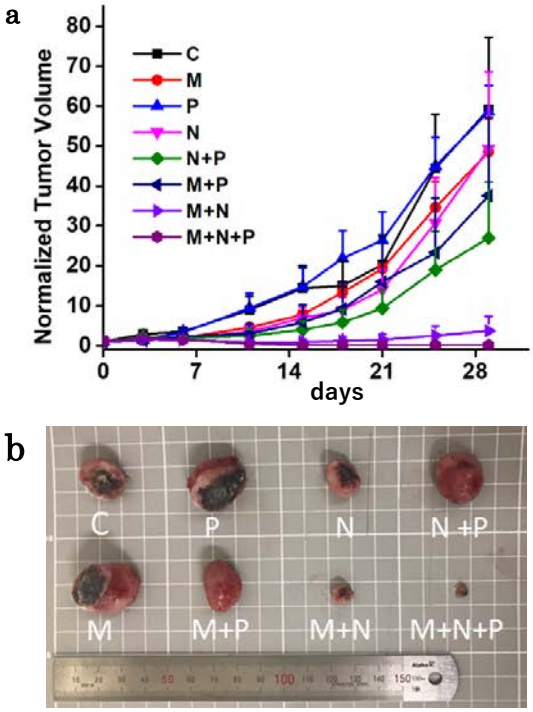

Fig. 1. Bimodal BNCT/PTT by **$^{10}B_4C$-PG**; (a) time coarse of tumor size (n = 3), (b) tumors after a month (C: control, M: $^{10}B_4C$-PG injection, P: 660 nm LED light irradiation, N: neutron irradiation) [3].

REFERENCES:

[1] M. Nishikawa *et al.*, Bull. Chem. Soc. Jpn., **94(9)** (2021) 2302-2312. [selected paper, highlighted at the inside cover].
[2] Y. Zou *et al.,* ACS Nano, **14(6)** (2020) 7216-7226.
[3] L. Zhao *et al.,* Angew. Chem.Int. Ed., **50(6)** (2011) 1388-1392. [highlighted atback cover].
[4] Y. Wang *et al.,* Small, **18(37)** (2022) 2204044.

CO6-17 Solution structure of intrinscially disordered protein

R. Inoue, T. Oda[1], and M. Sugiyama

Institute for Integrated Radiation and Nuclear Science, Kyoto University
[1]Department of Life Science, Rikkyo University

INTRODUCTION: It is considered that three-dimensional ordered structure is a prerequisite for maintain the proper development of protein's intrinsic function. In consistent with such common well-recognized knowledge, Wright and Dyson [1] for the first time reported that some proteins intrinsically lack three-dimensional ordered structure even under their functionally active state. At present, these proteins are known as intrinsically disordered proteins (IDPs) and play biologically significant biological roles, especially for those in Eukaryotes. Both high contents of hydrophilic and charged residues in IDP [2] make the destabilization of ordered structures, leading to its highly flexible structure in solution. It is considered the modulation of solution environment, such as temperature, ionic strength and so on, would affect the local configurations of above-described hydrophilic and highly charged residues. As a result, these changes in local scales could induce its overall structure as well. Among the parameters that can modulate solution environment, we especially focused on the effect of temperature change on solution structure and dynamics of IDP. In this work, we especially adopted small-angle X-ray scattering (SAXS) to analyze the ternary structures of IDP at different temperatures. As an example of IDP, we focused on intrinsically disordered region (IDR) of Hef (helicase- associated endonuclease for fork-structured DNA) (Hef-IDR) [3].

EXPERIMENTS: SAXS measurements were obtained on Photon Factory BL-6A (Tsukuba, Japan). The wavelength of the X-ray and the sample-to-camera distance were set to 1.5 Å and 2038.9 mm, respectively. The observed SAXS intensity was corrected for background, empty capillary and buffer scatterings, and transmission and converted to the absolute intensity using the scattering of water. All the data reduction was performed using the software "SAngler".

RESULTS: Figure 1 (a) shows the SAXS profiles at five different temperatures and no prominent change of SAXS profiles was observed with increasing the temperature. It means highly flexible configurations in solution state. We then calculated the temperature dependence of radius of gyration (R_g) utilizing the Guinier approximation and resulting temperature dependence of R_g is given in Fig. 1 (b). Interestingly, R_g decreased with increasing the temperature. It should be stressed that the globular proteins normally tend to lose higher-order structures with increasing temperature. Namely, the sensitivity of solution structure of IDP to the temperature change is totally different from that of globular one. Similar results were already reported by Uversky [2] as well, hence this

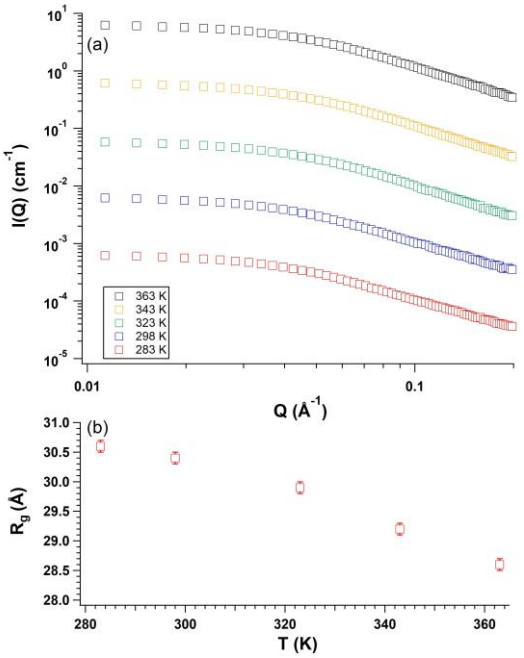

Fig. 1. (a) SAXS profiles of Hef-IDR at 283 K (red square), 298 K (blue square), 323 K (green square), 343 K (yellow square) and 363 K (black square), respectively. (b) Temperature dependence of R_g of Hef-IDR.

must be a characteristic feature of IDP. It is expected that a promotion of ordered structure with increasing temperature could be related to this experimental result. To figure out the possible mechanism of this singular result, we also started to study the dynamics of Hef-IDR in solution through quasielastic neutron scattering [4] which enables to analyze the internal of protein in solution.

REFERENCES:

[1] H. J. Dyson, P. E Wright., Curr. Opin. Struct. Biol. **12**, (2002) 54.
[2] V. N. Uversky, Protein J. **28**, (2009) 305.
[3] S. Ishino *et al*., J. Biol. Chem. **289**, (2014) 21627.
[4] R. Inoue *et al.*, Sci. Rep., **10**, (2020) 21678.

CO6-18 Oligomeric structure and interaction sites of Dpcd involved in actin bundle network formation

H. Koeda, K. Shinohara, K. Morishima[1], R. Inoue[1], M. Sugiyama[1] and M. Yohda

Department of Biotechnology and Life Science, Tokyo University of Agriculture and Technology
[1]Institute for Integrated Radiation and Nuclear Science, Kyoto University

INTRODUCTION: Cilia are organelles found on the surface of cells with hair-like protrusions. Cilia are classified into two types: motile cilia and non-motile cilia. Loss of function in motile cilia leads to primary ciliary dyskinesia (PCD). In knockout mice for the Dpcd gene, one of the causative genes for PCD [1,2], the actin bundle network, which is essential for ciliary movement, was not correctly formed in the cell surface layer. Previous studies showed that the Dpcd protein binds to actin and has the activity of bundling the fibers *in vitro*. The crystal structure analysis revealed the structure of the region from the 86th Glu to the 183rd Leu. The structure of this region showed a similar folding to small heat shock proteins. There is a characteristic positive charge cluster on the surface. The crystal structure analysis as well as structural prediction by alphafold2 suggested that K96, R107, and the region corresponding to basic amino acid residues from 185th to 191st is conserved in eukaryotes. Since the surface of actin is net negatively charged, the positive charge cluster region in the Dpcd is suggested to be involved in bundling F-actin. The fact that the concentration of Dpcd correlated with the actin-bundling activity means that oligomerization of Dpcd is necessary for activity acquisition. This study aimed to elucidate the oligomerization structure of Dpcd and the function of the positive charge cluster.

EXPERIMENTS: Mutant Dpcd genes were prepared by QuikChange method. Wild type and mutant Dpcd proteins with C-terminal His-tag were expressed in *E. coli* BL21(DE3) using pET15b vector. The *E. coli* lysate was applied on a Nickel column and Dpcd proteins were eluted with imidazole. After the removal of His-tag by thrombin, Dpcd proteins were purified by gel filtration using HiLoad 26/600 Superdex200. The affinity between actin and Dpcd proteins was examined by co-precipitation experiment with F-actin. The bundling of actin was observed by fluorescence microscopy using Rhodamine Phalloidin labelled actin. The oligomer structure of wild type Dpcd was examined by sedimentation velocity Analytical ultracentrifugation (SV-AUC).

RESULTS: Based on the structure model, we thought that Dpcd functions as a dimer or larger conformer (Fig. 1). Then, we analyzed the oligomeric structure of Dpcd wild type by AUC at various conditions (Fig. 2). Dpcd existed primarily as monomers or dimers. Although there was some change in the monomer and dimer equilibrium by the concentration and sample history, concentration dependent increase of dimer was not observed.
We conducted co-precipitation experiments between F-actin and wild-type or mutant Dpcd proteins, in which the basic amino acids on the surface were changed to acidic amino acids. Dpcd wild type was co-precipitated with F-actin, but the mutation in the positively charged surface region 1, which is predicted to be the binding site for F-actin, impaired the interaction. In contrast, mutations in the other region (region 2) did not affect the interaction. When we examined the actin-bundling activity, all mutants lost the activity. These results suggest that Dpcd binds to actin filaments by region 1 and that region 2 is required for the bundling.

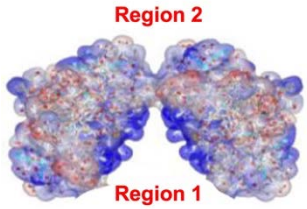

Fig. 1. Structure model of Dpcd tetramer

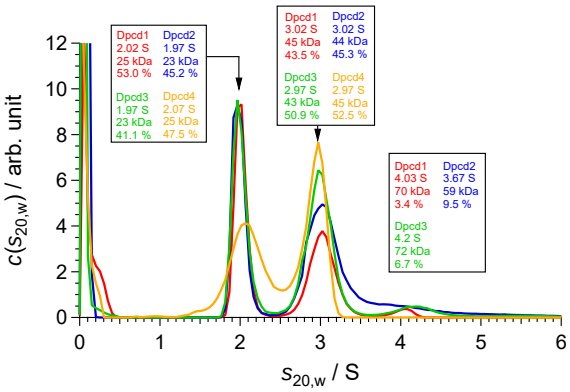

Fig. 2. SV-AUC results of Dpcd WT. Dpcd1: 1.5 mg/ml, Dpcd2: 15 mg/ml sample diluted to 1.5 mg/ml, Dpcd 3: 15 mg/ml sample diluted to 5 mg/ml, Dpcd 4: 1.5 mg/ml sample diluted to 0.3 mg/ml.

DISCUSSION: We had detected monomer and dimer of Dpcd in SV-AUC experiment. The basic amino acids on the surface of Dpcd were suggested to be involved in binding and bundling to actin.

REFERENCES:

[1] M. R. Knowles *et al.*, Am J Respir Cell Mol Biol., **30** (2004) 428-34.
[2] K. Shinohara *et al.*, Nat Commun., **3** (2012) 622.

CO6-19 Analysis of dinamic structure of intrinsically disordered protein

T. Oda, R. Oi[1], R. Inoue[2], K. Morishima[2], A. Okuda[2], M. Sugiyama[2], and M. Sato[1]

Department of Life science, Rikkyo University
[1]Graduate school of Medical Life science, Yokohama City University
[2]Institute for Integrated Radiation and Nuclear Science, Kyoto University

INTRODUCTION: Intrinsically disordered proteins (IDP), which do not have a rigid folded structure, play important roles in living cells. Because of its flexibility, it is difficult to solve its three-dimensional structure by X-ray crystallography or cryo-electron microscopy. Thus, it is hard to discuss its function based on its structure. Small-angle X-ray/neutron scattering (SAXS/SANS) is a useful method to analyze IDP because it provides structural information of IDP in an aqueous solution. In this study, we attempted to solve dynamic structures (various conformations in aqueous solution) of Hef with Ensemble Optimization Method (EOM) [1].

Hef is a protein involved in the repair of DNA damage. Hef consists of two folded domains (Helicase domain and Nuclease domain), which are connected by an intrinsically disordered region (IDR) [2]. In the previous study, we have shown that Hef tends to form aggregates (or oligomers) in aqueous solutions. The scattering data without contributions from aggregates, is required to determine the dynamic structure of Hef by EOM. For this purpose, we applied the AUC-SAS (analytical-ultracentrifugation and SAS) method [3] to the scattering data to remove contributions from aggregates.

EXPERIMENTS: The SAXS measurements were performed with BL15A2 installed at Photon Factory. The same sample solution (but not used for SAXS measurements) was used for AUC analysis. Prior to SAXS and AUC analysis, samples were subject to size exclusion chromatography to remove aggregates, and the protein concentration was adjusted to 0.5 mg/mL.

RESULTS: Since Hef tends to form aggregates (oligomers) at high protein concentrations, SAXS measurements were performed at low protein concentrations (0.5 mg/mL). AUC analysis showed that it contains a small amount of dimer. To obtain the scattering profile from monomeric Hef selectively, the AUC-SAS was applied to the observed SAXS profile. Fig. 1 shows the raw scattering data and the data after applying the AUC-SAS. The radius of gyration; R_g after applying AUC-SAS (45.6±0.9 Å) was slightly smaller than that from the raw data (46.2±0.9 Å).

Using the scattering profile of monomeric Hef, we attempted to solve the dynamic structure of Hef with EOM. EOM first created a large number of model structures (initial ensemble). Then, a small number of structure combinations (final ensemble) that can reproduce the experimental scattering curve were selected from the initial ensemble. Fig. 1(C) shows the final ensemble and the fraction of each structure. Hef showed highly flexible structure. The total fraction of compact structures in which the helicase domain and the nuclease domain are close together was relatively high (model 1 and 4, fraction 0.45 and 0.09). There were also extended structures (model 4, fraction 0.18) and intermediate structure between the extended and the compact (model 2 and 3, fraction 0.09 and 0.18). However, due to the high degree of structural freedom, the fraction of each structure cannot be accurately determined from SAXS data alone. Moreover, low contribution for scattering of IDR (consists of 100 amino acids, which is only 12.5% of Hef) makes it difficult to determine the detailed structure of IDR. Thus, further integrated analysis using SANS and molecular dynamics simulation is required.

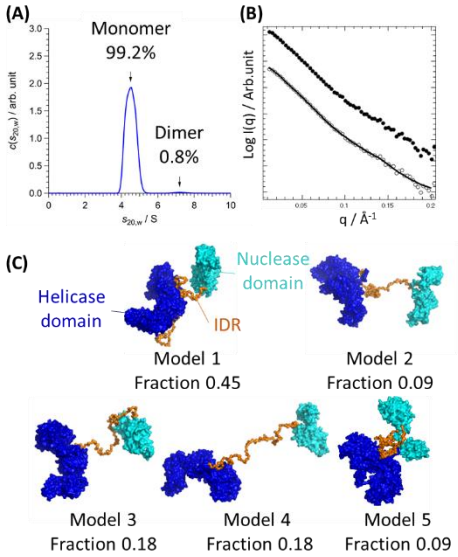

Figure 1. AUC-SAS and EOM analysis. (A) AUC analysis of Hef. (B) Raw scattering data (black filled circle), AUC-SAS (white circle), and back calculated scattering from final ensemble of EOM (black solid line). (C) Final ensemble of EOM.

REFERENCES:

[1] G. Tria *et al.*, IUCrJ. **26**(2015) 207-217.
[2] S. Ishino *et al.*, J. Biol. Chem. **289** (2014) 21627-21639.
[3] K. Morishima *et al.*, Commun Biol. **3** (2020) 294.

CO6-20 Interaction between Mint3 and FIH-1 involved in hypoxia stress responses

R. Maeda, S. Nagatoishi[1], K. Tsumoto[1], K. Morishima[2], R. Inoue[2], M. Sugiyama[2] and M. Hoshino

Graduate School of Pharmaceutical Sciences, Kyoto University

[1]Institute of Medical Science, the University of Tokyo
[2]Institute for Integrated Radiation and Nuclear Science, Kyoto University

INTRODUCTION: Oxygen is essential for many organisms to produce ATP efficiently from nutrients in food. Under the normal oxidative conditions, nutrients are metabolized through glycolytic pathway, tricarboxylic acid cycle and electron transport system. Temporal or local drop of oxygen level induces cells to change the metabolic pathway, which is known as hypoxia stress responses. The responses are mainly triggered by hypoxia inducible factors (HIFs) that activate transcription of a group of genes.

Under the normal oxygen conditions, transcriptional activities of HIFs in the cells are inhibited by the factor inhibiting HIF-1 (FIH-1). On the other hand, several cells including tumor cells and macrophages, metabolize nutrients exclusively by nonoxidative glycolytic pathway even under the normal oxygen levels. Munc-18 interacting protein 3 (Mint3) is recently found to activate the hypoxia responses by binding and inhibiting the activity of FIH-1 in these cells [1]. Although the N-terminal 214 residues (Mint3NT) are found to be necessary for the interaction with FIH-1 to inhibit its activity, little is known about inhibitory mechanisms.

We attempted to elucidate the molecular mechanism of the interaction between Mint3NT and FIH-1 by a various physicochemical methods, including small-angle X-ray scattering, analytical ultracentrifugation, and solution-state NMR.

EXPERIMENTS: High-expression systems for the N-terminal fragment proteins of Mint3 (Mint3NT) and smaller fragments (Mint3(1–117) and Mint3(101–214)), as well as full-length FIH-1 were constructed by E. coli BL21 strains. The proteins were expressed in bacteria grown in LB-broth and ^{15}N-enriched M9 minimal medium to produce unlabeled and ^{15}N-labeled proteins, respectively.

NMR experiments were performed on a Bruker Avance 600 spectrometer equipped with a triple-resonance probe. A typical ^{1}H-^{15}N HSQC experiments were performed at protein concentration of 50 μM. The solvent conditions used were 20 mM sodium acetate (pH 7.3), and 10% D_2O. The chemical shift value was referenced to DSS.

RESULTS: We measured the ^{1}H-15N HSQC spectrum of Mint3NT, and found that the dispersion of resonance peaks was very poor particularly along the ^{1}H-axis, suggesting the absence of strong hydrogen-bonding interactions (Figure 1). Furthermore, the superposition of two HSQC spectra separately recorded for the fragment proteins of Mint3NT (Mint3(1-117) and Mint3(101-214)) reproduced the spectrum of whole protein (Mint3NT), suggesting the absence of significant interaction between the N- and C-terminal regions of Mint3NT.

We also performed a titration experiment of ^{15}N-labled Mint3NT by unlabeled FIH-1, and found that the peak intensities for many residues were remarkably decreased in a concentration dependent manner. We analyzed several 3D-triple resonance experiments, and succeeded to unambiguously assign more than 95% of residues. By mapping the change in the peak intensity along the primary structure of the protein, we found that a broad range of residues were significantly affected by the addition of unlabeled FIH-1, suggesting the involvement of these residues in the interaction between Mint3NT and FIH-1.

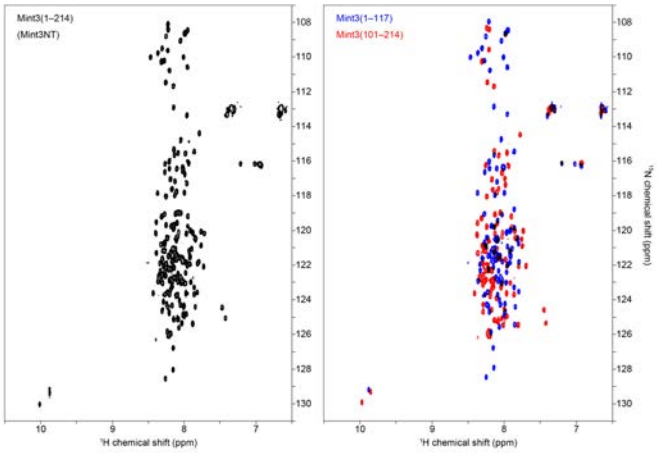

Fig. 1 ^{1}H-^{15}N HSQC spectra of Mint3(1–214) (left) and the superposition of fragment proteins (Mint3(1–117) and Mint3(101–214) (right).

We are now elucidating a change in overall dimensions of protein molecule upon complex formation between globular FIH-1 and intrinsically disordered Mint3NT by small angle X-ray scattering.

REFERENCES:

[1] T. Sakamoto *et al.,* Mol Cell Biol. **34 (1)** (2014) 30-42.

CO6-21 Analysis of novel p53-DBD aggregate for the development of anti-cancer drug

E. Hibino, R. Hijikata, K. Morishima[1], R. Inoue[1], M. Sugiyama[1] and H. Hiroaki.

Graduate School of Pharmaceutical Science, Nagoya University
[1]Institute for Integrated Radiation and Nuclear Science, Kyoto University

INTRODUCTION: The tumor suppressor protein p53 is a transcription factor that induces DNA repair proteins when DNA is damaged or induces apoptosis when DNA damage is severe, thereby preventing cells from turning cancerous. In fact, p53 mutations are found in half of all cancers, and preservation of p53 function is important in terms of cancer prevention. However, the development of therapeutic drugs targeting p53 has been challenging. It has been reported that the DNA-binding domain of p53 (p53-DBD) is aggregation-prone, that the introduction of hotspot mutations which are common in cancer increases its aggregation, and that the aggregates present heterogeneous [1,2].

We recently found that the environments in which amyloid aggregates and amorphous aggregates of p53-DBD tend to form are distinct [3]. They found that high salt and sugar concentrations inhibited amorphous aggregate formation of p53-DBD and suppressed loss of function. Inhibition compounds of aggregation of p53-DBD provides lead compounds for anti-cancer drugs that prevent loss of function of p53 [4], thus we constructed a screening system. Several compounds were evaluated and found to induce the formation of aggregates that are neither amorphous nor amyloid aggregates.

EXPERIMENTS: The p53-DBD protein solution was produced as a GST-fused form in an *E. coli* expression system. After GST-tag affinity purification, the GST-tag was cleaved with HRV3C protease and finally purified by size exclusion chromatography. 1 mg/mL p53-DBD protein solution with or without the addition of Compound A (Com. A) was incubated at 37°C for 1 h for DLS measurements.

DLS measured by using a system equipped with a 22-mW He-Ne laser, an Avalanche Photo Diode mounted on static/dynamic compact goniometer, ALV/LSE-5003 electronics, and ALV-5000 Correlator. Incident angles were 45°, 60°, 75°, 90°, 105°, 120°, and 135°, and measurements were taken three times at each angle.

RESULTS: The change in the size of p53-DBD aggregates with and without the addition of Com. A was investigated by DLS, and we found that as the amount of Com. A increased, the size of the aggregates increased. Furthermore, the heterogeneity of the aggregates decreased in proportion to the amount of Com. A.

There have been previous examples of compounds reducing the toxicity of aggregates, such as epigallocatechin gallate, which induces non-toxic oligomers rather than amyloid fibrils in the amyloid β protein [5,6]. We will further investigate the effect of this novel aggregate formation on p53-DBD function.

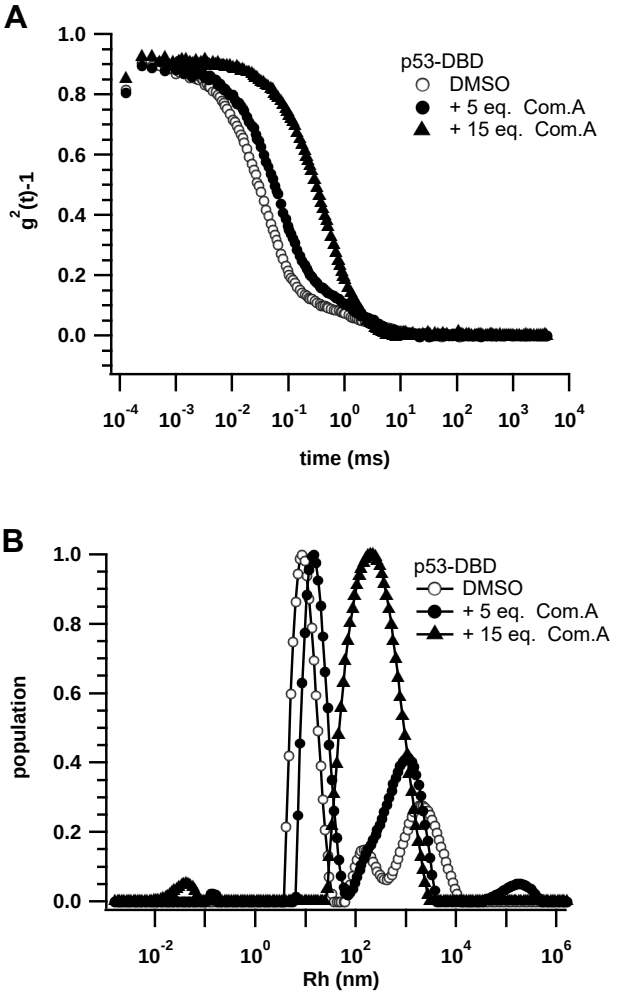

Fig. 1. Results of DLS measurements of p53-DBD aggregates without and with 5 and 15 equivalents of Com. A. (A) Auto-correlation function. (B) Histogram of hydrodynamic radius.

REFERENCES:

[1] A.P.D.A Bom *et al.,* J. Biol. Chem., **287** (2012) 28152-18162.
[2] S. Ghosh *et al.,* Cell Death Differ., **24** (2017) 1784-1798.
[3] E. Hibino *et al.,* Front. Mol. Biosci. **9** (2022) 869851.
[4] E. Hibino *et al.,* Biophys. Rev. **14** (2022) 267–275.
[5] Ehrnhoefer DE *et al.,* Nat. Struct. Mol. Biol. **15** (2008) 558-566.
[6] Bieschke J. *et al.*, Proc. Natl. Acad. Sci. **107 (17)** (2010) 7710-7715.

CO6-22 Analysis of the GATA3-nucleosome complex in solution

H. Tanaka[1], A. Okuda[2], K. Morishima[2], N. Sato[2], R. Inoue[2], M. Sugiyama[2] and H. Kurumizaka[1]

[1]*Laboratory of Chromatin Structure and Function, Institute for Quantitative Biosciences, The University of Tokyo*
[2]*Institute for Integrated Radiation and Nuclear Science (KURNS), Kyoto University*

INTRODUCTION:
In eukaryotes, genomic DNA is packaged into nucleosomes, the fundamental unit of chromatin structure. Nucleosome is the structure, in which about 150 base-pairs of genomic DNA are wrapped around a histone octamer composed of four core histones (H2A, H2B, H3, and H4). The nucleosome structure inhibits protein-DNA interactions including many transcription factors. However, a group of transcription factors called “pioneer transcription factors” is known to have the intrinsic ability to bind its target DNA motifs in the nucleosome. A pioneer transcription factor bound to the nucleosome may facilitate the recruitment of transcription factors and chromatin remodeling factors, which result in the change of the local chromatin structure.
The pioneer transcription factor GATA3 is a key regulator of developmental pathways including mammary epithelial cell differentiation and T cell development [1]. GATA3 is frequently mutated in breast cancer [2]. It has been reported that GATA3 binds to the target DNA motif in the nucleosome, and converts the chromatin structure from closed to open conformation [3]. However, it is still unknown how chromatin structure is changed by GATA3 binding. In this study, we performed analytical ultracentrifuge (AUC) and small angle X-ray scattering (SAXS) of GATA3-nucleosome complex to elucidate the structural change in nucleosome induced by GATA3 binding.

EXPERIMENTS:
The reconstituted nucleosome and the recombinant GATA3 DNA binding domain were mixed to form GATA3-nuclesome complex. The complex was purified by sucrose density gradient centrifugation to remove free GATA3. The quality of the purified sample was confirmed by non-denaturing PAGE and SDS-PAGE.
SAXS analysis was performed with a NANOPIX instrument (RIGAKU) at the Institute of Radiation and Nuclear Science, Kyoto University. We also performed AUC to correct the SAXS data by removing the SAXS profile portion derived from slight aggregates as previously described [4].

RESULTS:
We successfully purified the GATA3-nucleosome complex for AUC and SAXS analysis by sucrose density gradient centrifugation. AUC analysis confirmed the absence of free GATA3 and nucleosome in the purified GATA3-nucleosome complex fraction. On the other hands, AUC analysis showed the presence of aggregated components in the GATA3-nucleosome solution. SAXS analysis was then performed with the purified GATA3-nucleosome sample. Scattering profiles were calculated after removing the aggregated components in solution. Compared to the SAXS profile of nucleosome alone, the SAXS profile of the GATA3-nucleosome complex showed a difference, especially in the region larger than q=0.12Å^{-1}. This difference may be attributed to the increased molecular asymmetry induced by the GATA3 binding to the nucleosome.

REFERENCES:
[1] I. Ho *et al.*, EMBO J., **10** (1991) 1187-1192.
[2] B. Pereira *et al*., Nat. Commun., **7** (2016) 11479.
[3] M. Takaku *et al.*, Genome Biol., **17** (2018) 36.
[4] K. Morishima *et al*., Commun. Biol., **3** (2020) 294.

CO6-23 Measurement of the resistance of the spores of *Bacillus subtilis natto* to gamma radiation

T. Chatake, T. Saito, Y. Yanagisawa[1]

Institute for Integrated Radiation and Nuclear Science, Kyoto University
[1]Faculty of Pharmacy, Chiba Institute of Sciences

INTRODUCTION: It is well known that *Bacillus subtilis* has high resistance to ionizing radiation, because *Bacillus* forms spores [1]. *Bacillus* transform themselves into spores like seeds of plants, and the spores have high resistance to various severe conditions. On the other hand, vegetative cells of *Bacillus* are believed to have lower environmental resistance like other bacteria such as *Escherichia coli*. This radioresistance is completely different from that of radioresistant bacteria such as *Deinococcus radiodurans*, which has powerful molecular mechanisms that repair damaged DNA and protect proteins and lipids from radiation [2,3]. *B. subtilis* is a type species of *Bacillus*, and *B. subtilis natto* is one of the most famous subspecies of *B. subtilis*. It is used for the production of the traditional Japanese fermented food "natto", which contains biologically active substances: nattokinase [4], water-soluble vitamin K [5], and so on. The aim of this project is to elucidate the radioresistance of two forms (vegetative cell and spore) of *B. subtilis natto*. The two forms with the different resistances are expected to be useful for the breeding of this bacterium by gamma irradiation. The radioresistance of vegetative cells of *E. coli* has been studied in detail. In our previous study, we established an experimental procedure of to evaluate the radioresistance of *B. subtilis natto* in the same manner as that of *E. coli*, and measured the resistance of the vegetative cells to gamma radiation [6]. In the present study, the resistance of spores to gamma radiation.

EXPERIMENTS: The gamma irradiation experiment of *Bacillus subtilis natto* spores was performed out in the same manner as that of vegetative cells. The experimental protocol of the vegetative cells was previously reported in detail [6,7]. Glycerol stock of *B. subtilis natto* clone was incubated in 4 mL LB medium at 315 K with shaking (1200 rpm) for 65 h. After the incubation, 1 mL of the culture medium was centrifuged at 1,000×*g* for 10 min. After centrifugation, the supernatant was removed, and the precipitate was suspended in 1 mL Phosphate-buffered saline (PBS). The solution was heated at 353 K for 10 min in a dry block bath, in order to kill vegetative cells. Seven samples were prepared, and irradiated with gamma rays at doses of 0, 100, 200, 400, 800, 1600, and 3200 Gy at a dose rate of 10.8 Gy/min. After the irradiation, each solution was diluted with PBS, and plated. Colony formation units were counted after incubation for 8 h at 315 K.

RESULTS: As shown in Fig. 1, the resistance of the spores to gamma radiation was much higher than those of the vegetative cells. The radiation survival fraction curve of spore is a liner function, and the mean lethal dose (MLD) of spores was estimated to be 677.9 Gy. The high MLD value is expected from previous studies. On the other hand, the MLD of the vegetative cells was estimated to be 100.9 Gy, where the values at 0–50 Gy were excluded from the calculation. The difference between the two values indicates the dual nature of the resistance of *B. Subtilis natto* to gamma radiation. The MLD for the vegetative cells of *B. Subtilis natto* is close to that for *E. coli*. Meanwhile, the resistance to low radiation dose (0–50 Gy) observed in the vegetative cells of *B. subtilis natto*. was not observed in the case of the spores.

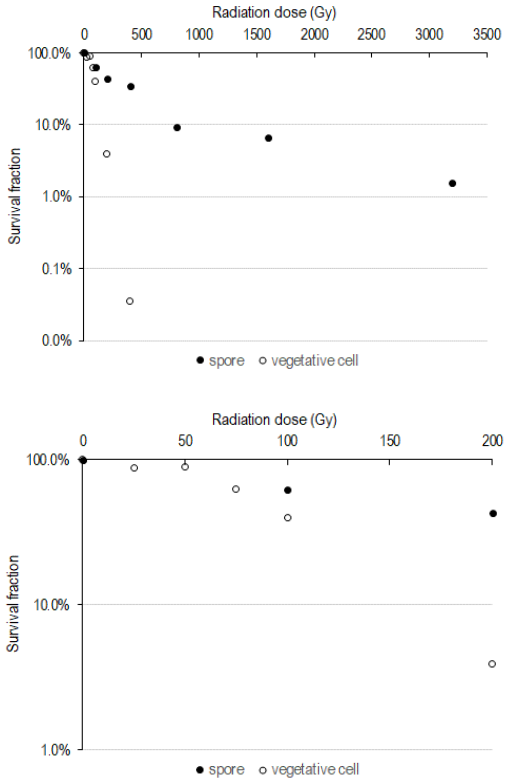

Fig. 1. The radiation survival fraction curve of *Bacillus subtilis natto* in the range of 0−3200 Gy (upper) and of 0–100 Gy (lower).

REFERENCES:

[1] P. Stelow, J. Appl. Microbiol., **101** (2006) 514−525.
[2] T. Saito, Viva Origino, **30** (2007) 85-92.
[3] A. Pavlopoulou *et al.,* Mutat. Res. Rev. Mutat. Res., **767** (2016) 92-107.
[4] H Sumi *et al.*, Experentia. **42** (1987) 1110-1111.
[5] H. Sumi *et al.,* Nippon Nogeikagaku Kaishi **73** (1999) 599-604.
[6] Y. Yanagisawa *et al.,* KURRI PROGRESS REPORT 2016, (2017) 65.
[7] T. Chatake *et al.,* Radiation biolo-gy research communications, **53** (2018) 280-290.

CO6-24 Analysis of water-soluble vitamin K complex from *Bacillus subtilis natto*

T. Chatake, A. Okoda, K. Morishima, R. Inoue, M. Sugiyama, T. Takata, Y. Yanagisawa[1]

Institute for Integrated Radiation and Nuclear Science, Kyoto University
[1]Faculty of Pharmacy, Chiba Institute of Sciences

INTRODUCTION: Vitamin K promotes bone formation; therefore, it is expected to suppress osteosis [1]. In addition, recent studies have reported that it also contributes to cardiovascular health [1]. Menaquinone-7 is a subtype of vitamin K_2 and is abundant in natto, a traditional Japanese food. Natto is produced from soybeans by fermentation using *Bacillus subtilis natto*. *Bacillus subtilis natto* produces a water-soluble macromolecular complex containing menaquinone-7, while menaquinone-7 alone is fatty-soluble. The molecular complex is of interest not only to researchers but also to companies because its solubility in water would be an advantage in nutritional, medical and pharmaceutical applications. However, the structure of the complex was not well understood. Ikeda and Doi reported that the complex was composed of peptides, and the main component was named K-binding factor (KBF) [2]. However, in the quarter of a century since this report, no further structural studies have been reported. In order to reveal the molecular structure of the complex in detail, the purification protocol of the complex was developed in our previous study [3]. The molecular weight was estimated to be ~100k, and the peptide of KBF was identified by Tris-Tricine SDS electrophoresis.

Recently, MALDI-TOF/MS of the complex shows strong peaks in the range of m/z = 1000 ~ 1100 [4], indicating that the molecular weight of KBF would be ~1k, while the previous electrophoresis suggested that the molecular weight would be ~3k [2,3]. It is an important question what are the properties of KBF: peptide length, amino acid composition, sequence, and so on. In the present study, the further analyses of KBF were carried out.

EXPERIMENTS: The water-soluble complex of menaquinone-7 (*Natto*-MK-7) was purified from the culture medium of *Bacillus subtilis natto* for several days [3]. During cultivation, *Bacillus subtilis natto* transform spores and releases cell contents into the medium in this process. The culture medium was concentrated and purified by repeating FPLC. *Natto-MK-7* was purified by triple or quadruple ion exchange chromatography (DEAE Sepharose FF) and then size exclusion chromatography (Sephacryl S300). The *natto*-MK-7 was assessed by the combination of size-exclusion chromatography and dynamic light scattering. Each fraction of size exclusion chromatography was analyzed by dynamic light scattering method.

MALDI-TOF mass spectrometry of *natto*-MK-7 was performed on a microflexLT MALDI-TOF mass spectrometer (Bruker Daltonics) in positive ion mode. Measurements were performed in the m/z ranges of approximately 300-4,000, 3,000-20,000, 20,000-201,500, and 820-14,000. Significant peaks were observed in the m/z range of 300-4,000, hence the subsequent measurement was performed only in this range. The standard amino acid analysis of *natto*-MK-7 was performed at the Instrumental Analysis Division, Global Facility Center, Creative Research Institution, Hokkaido University.

RESULTS: Fig. 1 shows the decay time of the main fraction of size-exclusion chromatography of *natto*-MK-7 used. A peak between 0.01 to 0.1 s corresponds to a single particle of *natto*-MK-7, of which hydrophobic radius (R_H) was estimated to be about 27 Å.

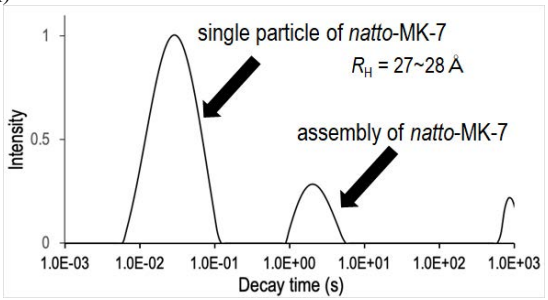

Fig. 1. The decay time of *natto*-MK-7 in DLS measurement.

For MALDI-TOF/MS and amino acid analysis, whole *natto*-MK-7 was used. Since KBF is the major component of *natto*-MK-7, the results could be considered as KBF-derived. As shown in Fig. 2, multiple peaks were found, indicating that KBF would be a 1k peptide with multiple sequence. In the amino acid analysis, hydrophilic amino acids: Asx (Asp or Asn) and Glx (Glu or Gln), and hydrophobic amino acids: Val and Leu, and small amounts of Met were found. The intervals are 14 in Fig. 2, which corresponds to a methyl group, supporting the results of MALDI-TOF/MS. Recently, KBF was extracted from natto MK-7 by reversed phase chromatography. The detailed analysis is on progress.

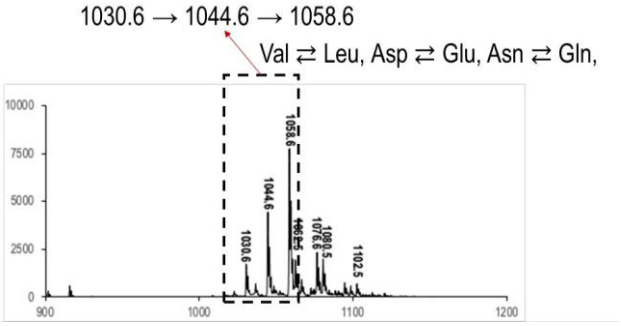

Fig. 2. The MALDI-TOF/MS chart of *natto*-MK-7.

REFERENCES:

[1] L.Wen *et al.*, Mol. Med. Rep. **18**, (1999) 3–15.
[2] H. Ikeda, Y. Doi, Eur. J. Biochem. **192**, (1990) 219-224.
[3] T. Chatake *et al.* J. Food Biochem. (2018) e12630.
[4] T. Chatake *et al.* KURNS PROGRESS REPORT 2019, (2020) CO6-20.

CO6-25 Preliminaly Study for The Development of New Treatment Method for Myxofibrosarcoma with BNCT

T. Fujimoto[1, 2], T. Andoh[3], T. Takata[4], Y. Sakurai[4]
H. Tanaka[4], M. Suzuki[4]

[1]*Department of Orthopaedic Surgery, Hyogo Cancer Center*
[2]*Department of Orthopaedic Surgery, Kobe University Graduate School of Medicine*
[3]*Faculty of Pharmaceutical Sciences, Kobe Gakuin Universityniversity*
[4]*Institute for Integrated Radiation and Nuclear Science, Kyoto University*

INTRODUCTION

Myxofibrosarcoma (MFS) is a rare malignant soft-tissue tumor observed predominantly in the extremities of elderly patients [1]. Since MFS is not sensitive enough to anticancer drugs or radiation therapy, wide surgical excision is the standard treatment for localized MFS. Nonetheless, this treatment affects, especially, the activity of daily life (ADL) of elderly patients. The present study explored the application of a more minimally invasive treatment with Boron Neutron Capture therapy (BNCT) with the use of a newly established human-derived MFS cell line-bearing animal model at the Institute for Integrated Radiation and Nuclear Science, Kyoto University (KURNS).

EXPERIMENTS

Newly established MFS cell line from a patient was used to create a cancer-bearing animal model by subcutaneously transplanting the MFS cells into the right thigh of nude mice. After the tumor grew, the animals were divided into a hot control group and a BNCT group. Only the BNCT group was administered BPA (500 mg/kg); almost 45 min thereafter, only the right lower limbs of both groups were irradiated with epithermal neutrons for 10 minutes. Immediately after termination of the animals, the tumor tissue was removed and subjected to histological examination.

RESULTS

The Newly established MFS cell line successfully formed tumors in the subcutaneous space of the nude mice. After irradiation, tumor regression was observed only in the BNCT group. Histological examination revealed destroyed tumor cells in a myxoid background of the BNCT group [Fig. 1], while tumor cells in the hot control group continued growing [Fig. 2].

FIGURES

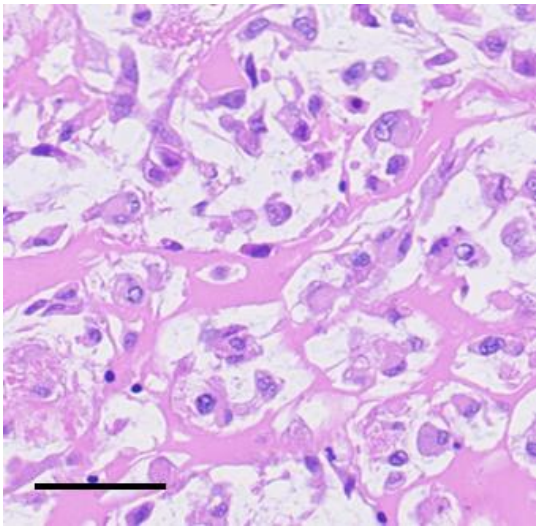

Fig. 1. Histopathological study (HE staining) of tissue from BNCT group reveals destroyed tumor cells in a myxoid background. Bar indicates 50μm.

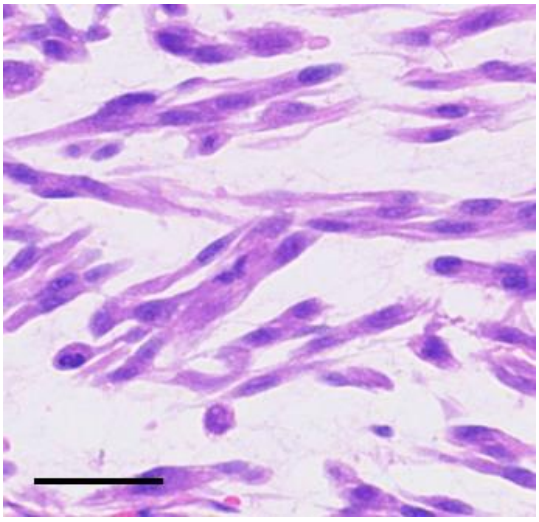

Fig. 2. Histopathological study (HE staining) of tissue from hot control group reveals no destroyed tumor cells. Tumor cells display a variably cellular spindle cell proliferation in a myxoid background. Bar indicates 50μm.

REFERENCE

[1] A. Gronchi *et al.,* Ann. Surg., **251** (2010) 506–511.

CO6-26 Development of Boron Cluster-Loaded Nanoparticles for BNCT

A. B. Fithroni,[1, 2] K. Kobayashi,[3] M. Akehi,[3] H. Inoue,[1]
S. Zhou,[1] T. F. N. Hakim,[1] H. Uji, [4] M. Ishimoto,[5]
M. Suzuki,[6] T. Ohtsuki,[1] and E. Matsuura[2, 3, 7]

[1] Department of Interdisciplinary Science and Engineering in Health Systems, Okayama University

[2] Department of Cell Chemistry, and [3]Collaborative Research Center for OMIC, Graduate School of Medicine, Dentistry, and Pharmaceutical Sciences, Okayama University

[4] Department of Material Chemistry, Graduate School of Engineering, Kyoto University

[5] Fukushima SiC Applied Engineering Inc.

[6] Institute for Integrated Radiation and Nuclear Science, Kyoto University

[7] Neutron Therapy Research Center (NTRC), Okayama University

INTRODUCTION: Boron neutron capture therapy (BNCT) is a novel nuclear therapeutic modality that can induce apoptosis in targeted cells, such as malignant cancer cells. To address the issues of limited application of clinically approved boron compounds, we designed self-assembling nanoparticles composed of polymeric micelles, namely, "Lactosome micelles" loaded with a boron cluster [1]. The particles consist of an amphipathic polydepsipeptide chain that are linked between a hydrophilic polysarcosine chain and a hydrophobic poly-L-lactic acid chain, and the polymer can assembly forms micelle-like particles. Moreover, the Lactosome micelles showed promising prospects for solid tumor accumulation via the enhanced permeability and retention (EPR) effect.

In the previous study, we aimed to develop Lactosome micelles highly loaded with a hydrophobic boron cluster that may be able to apply for the BNCT treatment [2]. In the present study, we performed *in vitro* and *in vivo* neutron irradiation to the AsPC-1 cells (human pancreatic cancer cells) and AsPC-1/CMV-Luc (their transfectant with luciferase expression) to assess BNCT effect of a boron cluster-loaded Lactosome micelles. The tumor growth was measured by bioluminescence imaging using IVIS.

EXPERIMENTS: For *in vitro* study, we irradiated AsPC-1 cells by subjected with 1 MW nuclear power for 30 min. After the neutron irradiation, colony formation assay of was performed by culturing in 60 mm dishes for 2 weeks. For *in vivo* study, the AsPC-1/CMV Luc cells-bearing mice were intravenously injected with a boron cluster-loaded Lactosome micelles, and then, the neutron irradiation was performed with nuclear power of 5 MW for 40 min. Data were represented as mean ± S.E.M. Significant differences were represented by *: $p < 0.05$.

RESULTS: In *in vitro* irradiation study, the results indicated that a boron cluster-loaded Lactosome micelles showed a significant inhibitory effect in the colony formation of the cancer cells (AsPC-1 cells) (Table 1). Furthermore, the *in vivo* irradiation study also showed that intravenous injection with a boron cluster-loaded Lactosome micelles and together with the neutron irradiation significantly suppressed the tumor growth on day 21 (after irradiation) (Table 2).

In conclusion, either *in vitro* or *in vivo* neutron irradiation studies suggest that our newly developed boron cluster-loaded Lactosome micelles are promising for boron compound candidates for BNCT.

Table 1. Effect of the neutron irradiation on *in vitro* colony formation of AsPC-1 cell treated with a boron cluster-loaded Lactosome micelles.

Group	Colony formation rate	
	0 min	30 min
Control (DPBS)	1	0.51 ± 0.01
Lactosome micelles	1	0.52 ± 0.03
-loaded with a boron cluster	1	0.14 ± 0.02*
BPA	1	0.30 ± 0.03*

Table 2. *In vivo* neutron irradiation study.

Group	Intensity (%) on day 21
Control (cold)	1129 ± 617
Control (hot)	774 ± 527
Lactosome micelles loaded with a boron cluster	177 ± 83.0*

Tumor growth in the xenografts with AsPC-1/CMV Luc cells were affected by the intravenously treated with a boron cluster-loaded Lactosome micelles and by the neutron irradiation. The tumor size was detected on day 21 after the irradiation.

REFERENCES:

[1] E. Hara *et al.,* Biochim. Biophys. Acta., **1830** (2013) 4046-4052.
[2] A.B. Fithroni *et al*., Cells, **11**(2022) 3307.

CO6-27 *C9orf72*-derived PR poly-dipeptides bind Kapβ2: discovery of secondary binding sites

E. Mori, T. Yoshizawa[1], T. Saio[2], K. Morishima[3], R. Inoue[3] and M. Sugiyama[3].

Department of Future Basic Medicine, Nara Medical University
[1]College of Life Sciences, Ritsumeikan University
[2]Institute of Advanced Medical Sciences, Tokushima University
[3]Institute for Integrated Radiation and Nuclear Science, Kyoto University

INTRODUCTION: Biomolecules such as proteins and nucleic acids form condensates in cells. These liquid-like condensates/droplets do not require membrane to keep boundaries, and thus are called membrane-less organelles. Because the process is partially explained in the context of physical chemistry, these phenomena are sometimes called biological phase separation or liquid-liquid phase separation (LLPS) in cells.

Uncontrolled phase separation is known to be associated with pathogenesis in some types of neurodegenerations. Repeat expansions in *C9orf72* cause amyotrophic lateral sclerosis (ALS) and front-temporal dementia (FTD), and the translated products, five poly-dipeptides, are thought to be the disrupters of physiological phase separations in cells, leading to cause protein aggregations. We found that Arg-rich poly-dipeptides, PRn and GRn, bound to proteins with low-complexity (LC) sequences, such as RNA-binding proteins, intermediate filaments, and FG-domains of nuclear pore complexes [1,2].

Further, we recently found that a phase modifier Kapβ2 [3] bound PRn and GRn through its nuclear localization signal (NLS) recognition motif at 1:1 ratio [4]. However, detailed mechanisms are still not clear.

EXPERIMENTS: To further analyze protein-protein interaction including weaker and dynamic affinities, analytical ultracentrifugation (AUC) was applied for complex formation of Kapβ2 and MBP-tagged PR18.

RESULTS: As shown in Fig. 1A, Kapβ2 bound at least two MBP-PR18 molecules and possibly up to 3 to 5 more MBP-PR18 bound, but not as strong as initial binding, suggesting that the affinity to the secondary binding site is weaker than that to NLS recognition motif. We made a mutant Kapβ2 that lacks potential binding sites of PRn, and found that mutant Kapβ2 could bind to only one MBP-PR18. These results suggest that Kapβ2 binds to PRn through NLS recognition motif and other specific region.

DISCUSSION: Further analysis such as NMR is required to understand detail mechanisms of Kapβ2-PRn complex formation.

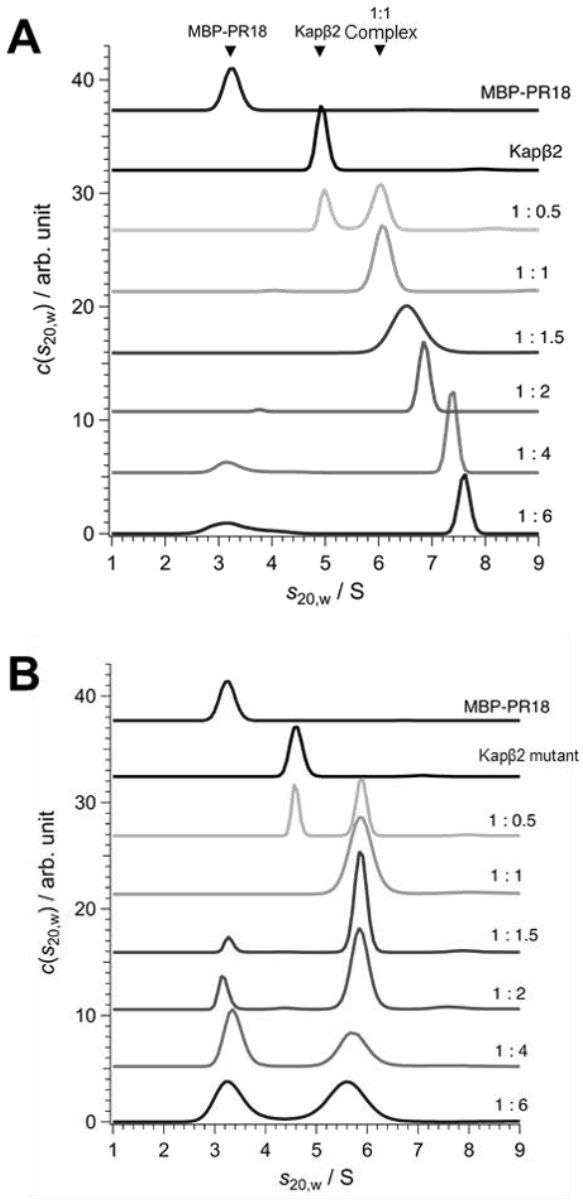

Fig. 1. AUC analysis of Kapβ2 and MBP-PR18 complex. Binding of multiple MBP-PR18 was analyzed with Wild-type Kapβ2 (A) and mutant Kapβ2 (B).

REFERENCES:

[1] Y. Lin *et al*., Cell, **167** (2016) 789-802.
[2] K.Y. Shi *et al*., Proc. Natl. Acad. Sci. U. S. A., **114** (2017) E1111-E1117.
[3] T. Yoshizawa *et al*., Cell, **173** (2018) 693-705.
[4] H. Nanaura *et al*., Nat. Commun., **12** (2021) 5301.

CO6-28 ^{11}C Medical-isotope Production via ^{12}C(γ,n)^{11}C Reaction with Carbon Nanotubes

N. Takahashi[1,2], M. Kurosawa[1], M. Tamura[1],
M. Fujiwara[1,2], T. Kubota[3], N. Abe[4], and T. Takahashi[4]

[1]*Research Center for Nuclear Physics, Osaka University*
[2]*Kyoto Medical Technology*
[3]*Agency for Health, Safety and Environment, Kyoto University*
[4]*Institute for Integrated Radiation and Nuclear Science, Kyoto University*

INTRODUCTION: L-[^{11}C]-Methionine is used as a positron emission tomography (PET) reagent for medical diagnosis of brain tumors [1]. The medical ^{11}C radioisotopes are mostly produced in a cyclotron via the ^{14}N(p,α)^{11}C reaction by bombarding enriched nitrogen gas with a proton beam [2]. In Japan, Hokkaido University and Osaka University have worked in collaboration with Sumitomo Heavy Industries to obtain the government permission for the PET examination with L-[^{11}C]-Methionine for checking the metastasis and recurrence test of the brain tumor patient [3,4].

Instead of producing ^{11}C with the cyclotron, we tried a novel method of producing ^{11}C using the bremsstrahlung γ-rays with a carbon nanotube (CNT) target to get a reasonable number of the ^{11}C activity.

EXPERIMENTS: Figure 1 shows the experimental scheme for the ^{11}C production via the ^{12}C(γ,n)^{11}C reaction. Bremsstrahlung γ-rays were produced by impinging a 40 MeV electron beam on platinum converter at the electron LINAC facility. The γ-rays were irradiated to CNT powders sealed in aluminum vessel with non-woven masks as gas inlet/outlet filter. The produced ^{11}C inside the vessel were oxidized to ^{11}CO or ^{11}CO$_2$ in O$_2$ gas, which was continuously flown during the irradiation. The ^{11}C gas (^{11}CO and ^{11}CO$_2$) were trapped in two 13X molecular sieve columns and 511-keV γ-rays from positron-electron annihilation were detected with CdZnTe detectors. Taking into account the incompleteness of trapping ^{11}C gas with molecular sieves, we prepared two molecular sieve columns to correct for the trapping efficiency.

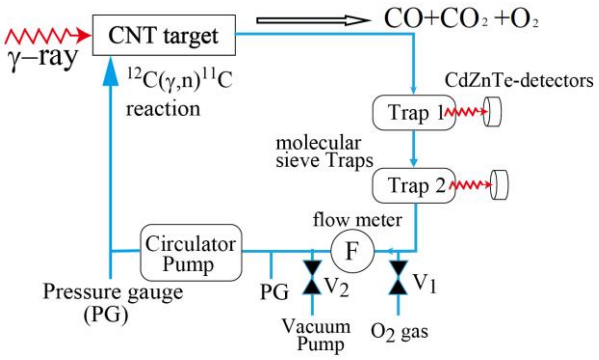

Fig. 1. Experimental scheme to produce ^{11}C and measure the extraction rate of ^{11}C gas.

In this experiment, single-walled carbon nanotube (SWCNT) powders (KH Chemicals Co., Ltd.) were irradiated under the different conditions of the bulk density of SWCNT powders, the pressure of O$_2$ gas in the vessel, and the flow rate of O$_2$ gas.

RESULTS: We confirmed that the ^{11}CO and ^{11}CO$_2$ flowed out from the vessel by observing 511-keV γ-rays from ^{11}CO and ^{11}CO$_2$ trapped in the molecular sieves. The measured decay curve obtained by measuring 511-keV γ-rays as a function of elapsed time was well in agreement with the ^{11}C half-life of 20 minutes.

The normalized activity of ^{11}C gas after the correction of the trapping efficiency for each experimental condition is summarized in Table 1. The normalized activity of ^{11}C gas was almost independent of the bulk density of SWCNT. On the other hand, the rate of ^{11}C gas reaching the trap column could increase by increasing the flow rate and pressure of O$_2$ gas. Further study is required to elucidate optimal production condition.

Table1. Normalized activity of ^{11}C gas for each condition.

Bulk density of SWCNT (mg/cm^3)	Flow rate of O$_2$ gas (cc/min)	Pressure of O$_2$ gas (MPa)	Normalized activity of ^{11}C gas (kBq/μA/g/min)
83.1	105	0.1	8.19±0.04
55.4	100	0.1	7.69±0.05
27.7	105	0.1	8.17±0.04
27.7	50	0.1	6.11±0.04
27.7	125	0.13	10.97±0.09

Biomass nanocarbon, graphene nano-powder and diamond nano-powder were also examined to achieve high yields of ^{11}C gas. The production yield of ^{11}C gas was as low as 7%, 24% and 72% that of SWCNT under the same experimental conditions, respectively.

Based on the experimental production rate of ^{11}C gas for SWCNT, we estimate that we can obtain the ^{11}C activity of 34 GBq when we use a SWCNT target under the conditions with 1) a length of 50 cm, 2) weight of 1.13 kg for 0.155 g/cm^3, 3) a 40 MeV electron beam intensity of 100 μA for 40 minutes bombardment. This 34 GBq radioactivity is enough amounts for one patient's diagnosis. The detailed report will be published in the near future [5].

REFERENCES:

[1] Y. Komatsu *et al.*, Radioisotopes, **67** (2018) 75.
[2] T. J. Ruth. A.P. Wolf, IEEE Trans., NS-26 (1979) 1710.
[3] M. Kinoshita *et al.*, J. Neurosurg **125** (2016) 1136.
[4] M. Kameyama *et al.*, Eur. J. Nucl. Med. Mol. Imaging, **43** (2016) 2267.
[5] M. Kurosawa *et al.*, to be published.

CO6-29 Molecular dynamics analysis of oxidative folding enzyme ER-60 with solution scattering measurement

A. Okuda, M. Shimizu, K. Morishima, Y. Yunoki, R. Inoue, N. Sato, R. Urade and M. Sugiyama

Institute for Integrated Radiation and Nuclear Science, Kyoto University

INTRODUCTION: ER-60, an oxidative protein folding enzyme, is a multi-domain protein, **a** and **a'** domains with catalytically active cysteine pairs and **b** and **b'** domains in the order **a-b-b-b'-a'**. In the process of oxidative protein folding, ER-60 might have the appropriate domain conformations and arrangement to function, and it is estimated that the structure fluctuates and changes according to the redox state of active cysteine pairs in the solution [1]. Inverse Contrast Matching Small-Angle Neutron Scattering (iCM-SANS) [2], which takes advantage of the large difference in neutron scattering length between hydrogen and deuterium, is useful for observing the dynamics and structures of such multi-domain proteins in solution.

When 75% deuterated and hydrogenated proteins are in 100% deuterated solvent, the deuterated proteins are scatteringly invisible, and only the hydrogenated proteins could be observed. Applying this method to multi-domain proteins, the domain of the hydrogenated domains could be selectively observed. To achieve this method for multi-domain proteins, the hydrogenated and deuterated domains must be prepared separately and then connected by the protein ligation technique.

To reveal the structure-function correlations of ER-60, we aim to analyze selective domain dynamics by iCM-SANS. The segmental deuterated proteins for this experiment were prepared by connecting the domains with the ligation enzyme *Oa*AEP [3].

EXPERIMENTS: The 75% deuterated recombinant protein was expressed in *E. coli* cultured in M9 medium containing 75% deuterium [4]. The recombinant proteins were purified using a His-tag affinity column and an ion exchange column. The deuterated and the hydrogenated domains were mixed in buffer containing 200 mM Tris-HCl (pH 7.4) / 150 mM NaCl. Then, 0.2 μM of the ligation enzyme *Oa*AEP was added to the mixture, and the protein ligation reaction was performed at 20°C for 64 hours. The results of ligation reactions were confirmed by SDS-PAGE. The deuteration rates of deuterated proteins were calculated by mass spectrometry with MALDI-TOF MS (microflexLT MALDI-TOF mass spectrometer, Bruker Daltonics) using a previously reported [3]. Analytical ultracentrifugation (AUC) experiments were performed at 60,000 rpm at 25 °C with a sedimentation velocity method using Rayleigh interference optics (ProteomeLab XL-I, Beckman Coulter). SAXS measurements were performed at 25 °C with 4 hours of exposure- time using a NANOPIX (Rigaku, Tokyo, Japan). The sample-to-detector distance (SDD) was set to 1330 mm and the q range was from 0.01 to 0.20 Å $^{-1}$.

RESULTS: The deuteration rates of deuterated **a** (*d*(**a**)) and **a'** (*d*(**a'**)) domains were calculated to be 73.5% and 74.1% respectively. The results of the protein ligation reaction are shown in Fig. 1. The band of ligation product, (*d*)**a**-(*h*)**bb'a'** and (*h*)**abb'**-(*d*)**a'**, connecting the deuterated and hydrogenated domains were observed, indicating the progress of the protein ligation reaction.

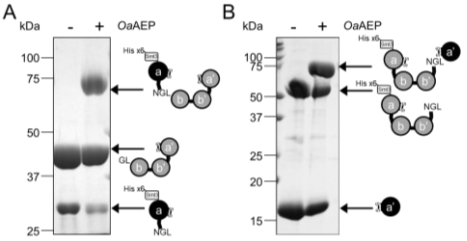

Fig. 1. The ligation products from (A) (*d*)**a** and (*h*)**bb'a'** domains and (B) (*h*)**abb'** and (*d*) **a'** domains of ER-60 by *Oa*AEP.

AUC was conducted to determine the abundance of monomers, aggregations, contaminations, and degradation products in the sample solution. It was shown that about half of (*d*)**a**-(*h*)**bb'a'** was degraded (Fig. A) and (*h*)**abb'**-(*d*)**a'** contained aggregation of 19% (Fig. B).

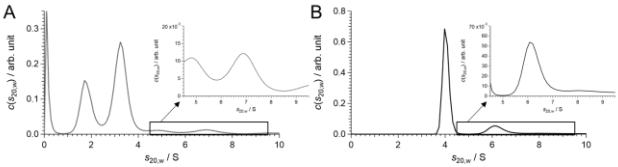

Fig. 2. Analytical ultra-centrifugation (AUC) profiles of ligation products, (A) (*d*)**a**-(*h*)**bb'a'** and (B) (*h*)**abb'**-(*d*) **a'**.

The SAXS profile of (*h*)**abb'**-(*d*)**a'** treated with AUC-SAS [5] is shown in Fig. 3.

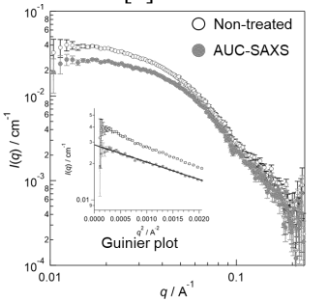

Fig. 3. The SAXS profiles of (*h*)**abb'**-(*d*) non-treated (white circles) and treated (gray circles) with AUC-SAS.

Currently, we are examining the conditions for obtaining the stable (*d*)**a**-(*h*)**bb'a'** sample, and are planning iCM-SANS measurements.

REFERENCES:

[1] A. Okuda *et al.*, Sci Rep., **11** (2021) 5655.
[2] M. Sugiyama *et al.*, J. Appl. Crystallogr., **47** (2014) 430-435.
[3] A. Okuda *et al.*, Angew Chem Int Ed Engl., **62** (2023) e202214412.
[4] A. Okuda *et al.*, Biophys Physicobiol., **18** (2021) 16-27.
[5] K. Morishima *et al.*, Commun Biol., **3** (2020) 294.

CO6-30 The regulation of the Kai proteins interaction by the KaiC hexamers that can adopt various kinds of phosphorylation states

Y. Yunoki, K. Morishima, N. Sato, R. Inoue, A. Okuda, R. Urade, M. Sugiyama

Institute for Integrated Radiation and Nuclear Science, Kyoto University

INTRODUCTION: Circadian rhythm is regulated by clock proteins. The cyanobacterial clock is controlled via interplay among KaiA, KaiB, and KaiC, which generate a periodic oscillation of KaiC phosphorylation in the presence of ATP. KaiC forms a homohexamer harbouring 12 ATP-binding sites and exerts ATPase activities associated with its autophosphorylation and dephosphorylation. Although there are as many as 700 phosphorylation states could become in the KaiC hexamer due to the presence of two phosphorylation sites in the subunit KaiC, previous reports disclose only the average phosphorylation state of the KaiC hexamer in solution. Herein, in order to understand the oscillation mechanism involved in the clock proteins, we develop the native mass spectrometry for simultaneous analyzing of the phosphorylation states in the KaiC hexamer and Kai proteins interaction as exemplified KaiA-KaiC interaction.

EXPERIMENTS: nMS measurements were recorded on a microTOF II ESI mass spectrometer (Bruker) at room temperature using the microTOF II software. KaiA and KaiC originating from thermophilic cyanobacteria, *T. elongatus* BP-1, were expressed in *Escherichia coli* and purified by an anion-exchange column (Resource Q) and size-exclusion column (superdex75). To control the phosphorylation state in the KaiC hexamer, we used two KaiC mutants, $KaiC_{AA}$ and $KaiC_{DD}$ (in which Ser431 and Thr432 were both substituted with aspartate and alanine residues, respectively), mimicking the dephosphorylated and phosphorylated states of KaiC, respectively. For preparing the group of heterogeneous phosphorylation state in the KaiC hexamers, before adding ATP, we mixed unlabeled $KaiC_{AA}$ mutant and ^{13}C labeled $KaiC_{DD}$ subunit. In this way, there are seven types of the KaiC hexamers with different phosphorylation states in solution.

RESULTS: We successed in preparation of the group of heterogeneous phosphorylation state in the KaiC hexamer (Fig. 1A). Then, we tried to reveal the KaiA-KaiC interaction by adding KaiA in this KaiC group.

As shown in Fig. 1B, our data indicate the KaiA-KaiC interaction depends on the number of $KaiC_{AA}$ in the KaiC hexamer. It means that KaiA-KaiC interaction might be controlled by the phosphorylation state in the KaiC hexamer.

To examine the possible dependence of KaiA–KaiC interaction on the phosphorylation state in the KaiC hexamer, we measured nuclear magnetic resonance (NMR) of KaiC.

NMR data show only the subunit $KaiC_{AA}$ in the KaiC hexamer released the intrinsically disordered region and becomes reactive with KaiA, leading to the enhanced KaiA–KaiC interaction.

We illustrated KaiC regulates KaiA-KaiC interaction by changing the phosphorylation state in the KaiC hexamer. We believe that these insights will contribute to the understanding of the oscillation mechanism through the dissociation and assembly of Kai proteins.

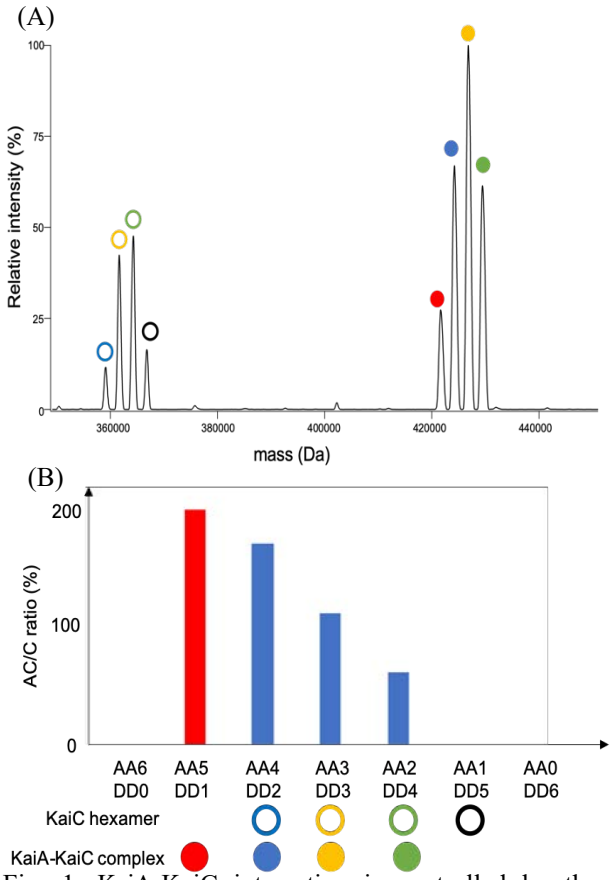

Fig. 1. KaiA-KaiC interaction is controlled by the phosphorylation state in KaiC hexamer.

(A) Native mass spectra of heterogeneous phosphorylation state in KaiC hexamer in the presence of KaiA. The open circles show the KaiC hexamer, and the closed circles show the KaiA-KaiC complex. The red, blue, yellow, green and black circles show the KaiC hexamer which is composed of 1 : 5, 2 : 4, 3 : 3, 4 : 2, 5 : 1 of $KaiC_{AA}$ and $KaiC_{DD}$.

(B) Plot of relative peak intensity of KaiA-KaiC complex versus KaiC. The color of the peak, that yielded only KaiA-KaiC complex, is red.

CO6-31 Small-angle scattering analysis of wheat protein glutenin

N. Sato, R. Urade, A. Okuda, M. Shimizu, K. Morishima, R. Inoue, and M. Sugiyama

Institute for Integrated Radiation and Nuclear Science, Kyoto University

INTRODUCTION: Food science in combination with quantum beam analyses is now attracting wide attention among researchers. Food materials have been difficult to examine their structure because they have undesirable characteristics for structural analyses, such as condensed, amorphous, opaque and multi-component features. However, quantum beam analyses are successfully applicable to those kinds of materials such as colloids, rubbers, gels, and other soft matters. It is therefore expected that quantum beam analyses can also be powerful tools for examining the structural of food materials, which has not been closely investigated by conventional methods.

There are many kinds of wheat flour foods such as bread and noodle. These foods are produced from wheat dough, which is prepared by kneading wheat flour with water and salt. Physical properties of the dough are responsible for the quality and processability of wheat flour foods. Gluten, a composite of major wheat storage proteins gliadin and glutenin, makes a significant contribution to the physical properties of wheat dough. Gliadin is a monomeric protein and exhibits viscose feature while glutenin is high-molecular-weight network protein and exhibits elastic feature. In order to clarify the properties of gluten composite, it is required to investigate the individual properties of each protein gliadin and glutenin.

Conventionally, gliadin had been extracted only with alcohols or acids. However, we found gliadin can be extracted with pure water from the dough containing NaCl. This finding enabled us to investigate the structure of gliadin in conditions closer to actual foods. It was revealed in our previous study [1] that gliadin monomers are isolated and dispersed at a low concentration of aqueous solution, but with increasing gliadin concentration, they associate together gradually to form multimolecular domains. At higher concentrations, on the other hand, gliadin is no longer soluble in water and form aggregates with density fluctuation inside. The correlation length of this fluctuation becomes smaller with increasing gliadin concentrations. Another finding is that the structure of gliadin hydrates is greatly affected by salts. The correlation length of density fluctuation becomes smaller with increasing NaCl concentration, indicating that gliadin hydrates are contracted by NaCl.

Thus we could successfully reveal the structure of gliadin. However, the structure of glutenin has not been clarified yet. Glutenin is a protein with completely different characteristics from gliadin. Therefore it is expected that the nano-structure of glutenin is also largely different from that of gliadin. In this study, we carried out SAXS measurements on glutenin hydrates and investigated the difference from the gliadin structure.

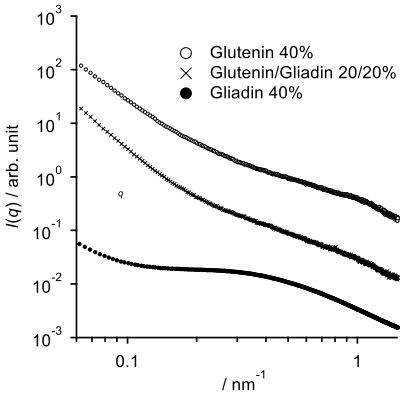

Fig. 1. SAXS profiles of glutenin, gliadin and their mixture.

EXPERIMENTS: Glutenin was obtained from the insoluble residue after gliadin preparation. Glutenin concentration was 40 wt%. SAXS measurements were performed with a laboratory SAXS instrument (NANOPIX, Rigaku) installed at Institute for Integrated Radiation and Nuclear Science, Kyoto University. The wavelength of X-ray was 1.54 Å and the camera length was 1300 mm. All measurements were carried out at 25 °C.

RESULTS: Fig. 1 shows the SAXS profiles of 40 wt% hydrates of glutenin, gliadin, and their 1:1 mixture. Gliadin shows gentler upturn in the low-q region and a broad peak around 0.3–0.6 nm^{-1}. As reported before, this result demonstrates that gliadin forms aggregates with density fluctuation inside. In other words, gliadin molecules gather together but dense and sparse regions are present within the aggregates. In contrast, glutenin shows steeper upturn in the low-q region and a small peak appears around 1 nm^{-1}. The slope in the low-q region has nearly q^{-4} dependence, indicating that a definite interface of large aggregates of glutenin is found. This result is explained by the structural difference of glutenin and gliadin. Glutenin is a high-molecular weight protein with network structure via disulfide bonds. Consequently, it forms huge aggregates in the hydrates. On the other hand, gliadin is a monomeric protein and associates each other more weakly by hydrophobic interaction. Hence it forms aggregates not so large as glutenin. The structure of the 1:1 mixture is similar to that of glutenin. This is because the molecular weight of glutenin is much higher than gliadin. In principle, scattering intensity is proportional to the square of the molecular weight. Accordingly, the profile of the mixture strongly reflects the high-molecular-weight glutenin.

REFERENCES:

[1] N. Sato *et al.,* J. Agric. Food Chem., **63** (2015) 8715.

CO6-32 Design, Synthesis, and BNCT Effect of Macrocyclic Polyamine-type Boron Carriers for BNCT

S. Aoki[1,2], H. Ueda[3], M. Suzuki[3], Tanaka, T.[1,4] S. Masunaga[3], N. Kondo[3], and Y. Sakurai[3]

[1]*Faculty of Pharmaceutical Sciences, Tokyo University of Science*
[2]*Research Institute for Science and Technology, Tokyo University of Science*
[3]*Institute for Integrated Radiation and Nuclear Science, Kyoto University*
[4]*Faculty of Pharmaceutical Sciences, Okayama University*

INTRODUCTION: Neutron capture therapy using boron-10 (^{10}B) (BNCT) is one of powerful therapies for local tumor control in the treatment of brain tumor, melanoma, and related diseases [1].

Based on high intracellular uptake pendant-cyclen (cyclen = 1,4,7,10-tetraazacyclododecane) in cancer cell, we designed and synthesized several phenylboronic acid-pendant 9-, 12-, and 15-membered macrocyclic amines such as **^{10}B-1a~3a** and their corresponding Zn^{2+} complexes **^{10}B-1b~3b** (Fig. 1) [2]. The experimental results suggest that the metal-free **^{10}B-1a~3a** are introduced into cancer cells (A549 and HeLa S3 cells) more efficiently than their Zn^{2+} complexes **^{10}B-1b~3b** with considerably high cancer/normal cells selectivity. Besides, it was found that 12- and 15-membered derivatives **^{10}B-2a~3a** exhibit a higher BNCT effect than **^{10}B-1a**, possibly because **^{10}B-2a~3a** form the corresponding Zn^{2+} complexes **^{10}B-2b~3b**, which strongly interact with DNA in living cells, resulting in the efficient breakdown of DNA double-strand upon the neutron irradiation.

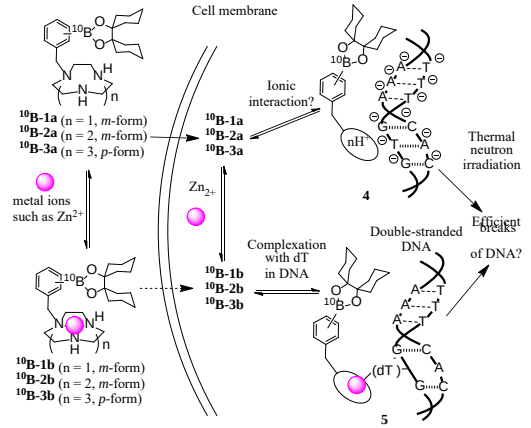

Fig. 1. Structures of boron-containing macrocyclic polyamines and the corresponding Zn^{2+} complexes and the proposed scheme of their intracellular uptake and interaction with DNA for BNCT.

EXPERIMENTS and RESULTS: The synthesis of **1a~3a** and their Zn^{2+} complexes **1b~3b** was carried out and their cytotoxicity and cellular uptake activity against cancer cell lines (HeLa and A549 cells) and normal cell line (IMR-90) were evaluated. It was found that the intracellular uptake of **1~3** is higher than that of BSH and BPA, possibly via polyamine transporter system (PTS) and that **^{10}B-2a**, **^{10}B-3a** **^{10}B-2b**, and **^{10}B-3b** exhibit more potent BNCT effect than that of BSH and BPA.

These results have prompted us to design and synthesize boron carriers that have homo- and heterodimeric macrocyclic polyamines functionalized phenylboronic acid units such as **4a~5a** (homodimers) and **6a~8a** (heterodimers) and their corresponding Zn^{2+} complexes **4b~8b** (Fig. 2), because it was well established that polymeric Zn^{2+} complexes would form more stable complexes with DNA double strand than monomeric Zn^{2+} complexes than monomeric Zn^{2+} complexes [3].

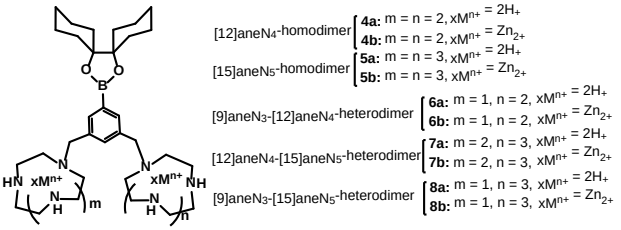

Fig. 2. Structures of boron-containing dimeric macrocyclic polyamines and Zn^{2+} complexes (**4a~8a** and **4b~8b**).

It has been found that the intracellular uptake and BNCT of ^{10}B-enriched **4a~8a** and **4b~8b** are lower than that of **1~3** (Fig. 3), possibly due to their high hydrophilicity than **^{10}B-2a** [4,5]. Our next work will be the synthesis of monomeric polyamines that are equipped with multiple boron units for more efficient BNCT effect and the observation of these B-containing agents in nucleus.

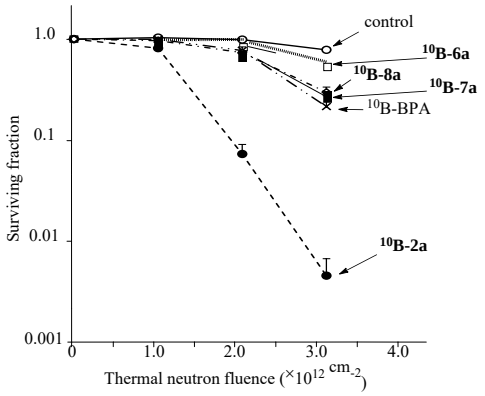

Fig. 3. Antitumor effect of ^{10}B-enriched BPA, **2a, 6a, 7a,** and **8a** (100 μM) against A549 cells upon irradiation with thermal neutron (averaged thermal neutron flux was 1.2~1.3 X 10^9 n/cm^2·s), as evaluated by a colony assay.

REFERENCES:

[1] a) R. F. Barth *et al.*, Clin. Cancer Res., **11** (2005) 3987-4002. b) R. F. Barth *et al.*, Rad. Oncol., **7** (2012) 146-166.
[2] H. Ueda *et al.*, J. Med. Chem., **64** (2021) 8523-8544.
[3] S. Aoki and E. Kimura, Chem. Rev., **104** (2004) 769-788.
[4] H. Ueda *et al.*, Eur. J. Inorg. Chem., **2022** (2022) e202100949 (24 pages).
[5] S. Aoki *et al.*, In "*Characteristics and Applications of Boron*" 2022, pp 83-105, Charchawal Wongchoosuk, Ed., IntechOpen, Croatia.

CO6-33 Radiolabeling of composite natural material chicken eggshell membrane via neutron irradiation $^{6}Li(n,\alpha)\ ^{3}H$ reaction

M. Shimizu[1], E. Fujita[1], N. Nogawa[2], K. Takamiya[3] and Y. Atomi[1]

[1]*Material Health Science, Tokyo University of Agriculture and Technology*

[2]*Isotope Science Center, The University of Tokyo*

[3]*Institute for Integrated Radiation and Nuclear Science, Kyoto University*

Chicken eggshell membrane (ESM) has been listed as an excellent wound-healing agent in Chinese pharmacopoeia book entries for 400 years. It is a non-woven fabric composed of fibrous biopolymers that are mainly protein-based and contain a large amount of extracellular matrix such as collagen and proteoglycans, as well as antibacterial proteins, cross-linked by lysyl-oxidase. Recently, proteomic analysis has revealed that it contains more than 400 different proteins. We previously found that hydrolyzed ESM provide young extracellular environment to dermal fibroblast [1] and improved skin elasticity and reduced facial wrinkles when topically applied as cosmetics [2]. Ingestion of this non-woven fabric has been reported to improve pain in knee joints and prevent liver fibrosis and ulcerative colitis in animal experiments. In our previous studies, we have found that eggshell membrane supplements improved skin elasticity, respiratory function, and locomotion (especially balance function) in healthy adults within 8 weeks of taking the supplements [3]. ESMs are secreted by cells in the narrow oviduct of the parent bird and serve as a biomineralization scaffold for eggshell formation and to protect chick embryo from drying and infection. We applied the tritium labeling of organic compounds via the 6Li(n,α)3H reaction, which has been used for radiolabeling of natural products that are difficult to synthesize and for tissue distribution in individuals, to ESM and conducted pilot experiments to determine whether ingested ESM are indeed digested and absorbed and distributed to various tissues. The labeled eggshell membrane was orally administered to mice, and was digested and absorbed. The radioactivity derived from the labeled ESM was detected in blood 2 hours after administration, peaking 6 hours later, and was also detected in almost all tissues [4]. However, in the previous irradiation experiment with JRR-4 (3.5 MW, 20 min), many parts of the sample were scorched, and the optimization of the eggshell membrane to lithium carbonate ratio and irradiation conditions remained an issue. In this study, in order to obtain tritium-labeled eggshell membranes for detailed verification of the pharmacokinetics and cellular uptake of ESM orally ingested by mice, we irradiated ESM powder samples (Almado Inc.) sealed in quartz glass (Figure 1) under milder conditions (Pn-2, 1 MW, 70 min). As a result, tritium labeling was successful and discoloration of the samples was minor. The Kyoto University furnace is beneficial for irradiating protein samples because its low power output does not raise the sample temperature during irradiation. On the other hand, since the labeling efficiencies of the two samples were different, it is necessary to monitor the actual irradiation efficiencies in the future experiment.

Fig.1 ESM powder in the custom-made quartz tubes.

REFERENCES:

[1] E. Ohto-Fujita *et al.,* Cell Tissue Res., **345** (2011) 177-190.
[2] E. Ohto-Fujita *et al.,* Cell Tissue Res., **376** (2019) 123-135.
[3] E. Ohto-Fujita *et al.,* J. Fiber Sci. Technol., **77** (2021) 258-265.
[4] E. Ohto-Fujita *et al.,* J. Fiber Sci. Technol., **77** (2021) 182-187.